Physics of Fluids

Computational fluid radiative dynamics of the Galileo Jupiter entry

Cite as: Phys. Fluids **31**, 106104 (2019); https://doi.org/10.1063/1.5115264
Submitted: 20 June 2019 . Accepted: 24 September 2019 . Published Online: 15 October 2019

L. Santos Fernandes, B. Lopez, and M. Lino da Silva

COLLECTIONS

F This paper was selected as Featured

View Online Export Citation CrossMark

AIP Publishing

Phys. Fluids **31**, 106104 (2019); https://doi.org/10.1063/1.5115264 **31**, 106104

Physics of Fluids ARTICLE scitation.org/journal/phf

Computational fluid radiative dynamics of the Galileo Jupiter entry

Cite as: Phys. Fluids 31, 106104 (2019); doi: 10.1063/1.5115264
Submitted: 20 June 2019 • Accepted: 24 September 2019 •
Published Online: 15 October 2019

L. Santos Fernandes,[1,a)] B. Lopez,[2,b)] and M. Lino da Silva[1,c)]

AFFILIATIONS

[1] Instituto de Plasmas e Fusão Nuclear, Instituto Superior Técnico, Universidade de Lisboa, Av. Rovisco Pais, 1049–001 Lisboa, Portugal
[2] Department of Aerospace Engineering, University of Illinois at Urbana-Champaign, 306 Talbot Lab, 104 S. Wright St., Urbana, Illinois 61801, USA

[a)] **Electronic mail:** luis.fernandes@ist.utl.pt
[b)] **Electronic mail:** belopez@illinois.edu
[c)] **Electronic mail:** mlinodasilva@tecnico.ulisboa.pt

ABSTRACT

On December 7th, 1995, the Galileo descent probe entered Jupiter's atmosphere at a relative velocity of 47.4 km s^{-1}. Flight data revealed an unforeseen recession profile: while the stagnation region had been significantly oversized, the shoulder almost completely ablated. In an attempt to understand why numerical predictions diverge from the flight data, several sensitivity studies were performed at the 180 km altitude point. The inaccuracy of the Wilke/Blottner/Eucken model at temperatures above 5000 K was confirmed. When applied to Galileo's entry, it predicts a narrower shock with higher peak temperatures compared to the Gupta/Yos model. The effects of He and H_2 line-by-line radiation were studied. Inclusion of these systems increased radiative heating by 9% at the stagnation point, even when precursor heating is unaccounted for. Otherwise, the internal excitation of H_2 due to absorption of radiation originating from the highly emitting shock layer promotes H_2 emission before dissociation occurs at the shock, yielding 196% higher radiative heat fluxes. This emphasizes the importance of H_2 radiation not only on the recession experienced by Galileo but also for future entries in gas giants. Accordingly, thermal nonequilibrium resulted in 25% lower radiative heating when compared to an equilibrium solution, contrary to previous investigations that neglected H_2. Ablation products absorption was shown to counteract the increased emission due to precursor heating of H_2. However, the ablation layer temperature must be accurately predicted using a material-response code coupled to the flowfield since radiative heating has been shown to significantly depend on this energy-exchange interaction. Finally, the tangent-slab and ray-tracing models agreed to within 12%.

I. INTRODUCTION

On October 18, 1989, the Galileo orbiter was sent aboard the cargo bay of the space shuttle Atlantis, carrying a descent probe designed to penetrate the Jovian atmosphere with a set of scientific instruments. After a six year orbit through the Solar System, the probe officially began its descent at a relative velocity of 47.4 km s^{-1} on December 7, 1995. During a 30 s period, the probe decelerated from Mach 50 to under Mach 1, having reached a maximum deceleration of 250 g, while experiencing peak heating rates exceeding[1,2] 300 MW m^{-2}. The extreme heating environment experienced by the probe during its descent remains, until today, one of the most severe ever encountered by a planetary entry capsule.

The descent probe's thermal protection system (TPS) sphere-cone geometry is shown in Fig. 1. The 339 kg probe was equipped with 10 ablation sensors (ARAD, A_{1-10}) and four resistance thermometers (T_{1-4}) for collecting data during entry. Although the mission was a success, postflight data analysis revealed how close the entry probe's TPS came to completely ablate near the shoulder.[3] Despite the efforts undertaken during preflight mission preparation to simulate the flowfield around the entry probe, the predictions have since been confirmed to present large differences with the flight data, mainly when it comes to the predicted recession of the heat

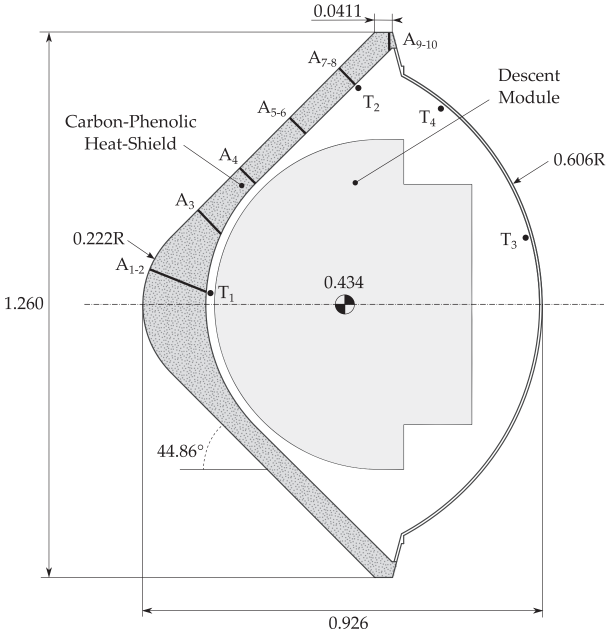

FIG. 1. Galileo probe geometry and sensor locations.

shield. This has spurred a revival of research aimed at understanding the causes of these discrepancies, while at the same time increasing the confidence on future predictions regarding TPS sizing. This will allow scientists and engineers to redirect part of the heat shield's mass toward scientific equipment, increasing the available payload and cost-effectiveness of future missions.

The present work aims to understand the origin of such discrepancies. Accordingly, a set of thorough sensitivity studies regarding the modeling of different phenomena that have been either neglected or inadequately modeled in the past has been conducted. Specifically, the impact of modeling transport properties using the Wilke/Eucken/Blottner or the Gupta/Yos models in the context of H_2–He mixtures is assessed, thermochemical nonequilibrium is considered, inclusion of He and H_2 in the radiative analysis is studied, and the tangent-slab approximation for radiative transfer is compared to the ray-tracing approach. This is accomplished by first solving the flowfield using the SPARK computational fluid dynamics (CFD) Fortran solver,[4] after which the radiative field is computed using the SPARK Line-by-Line (SPARK LbL) Matlab code[5–7] (formerly known as SPARTAN) in a decoupled fashion. Whenever possible, the Tauber-Wakefield correlation[8] is considered to account for flowfield-radiation coupling. Finally, the influence of precursor heating and ablation products injection in the presence of H_2 is discussed and estimated at the stagnation point in an approximate manner, using results from previous studies on these phenomena. Hence, the goal of the present work is not to attempt to directly estimate the heat fluxes experienced by Galileo, as that would require an accurate accounting of ablation products-flowfield interactions, precursor heating modeling, and flowfield-radiation coupling, all of which have a profound impact on the flowfield. Rather, the aim is to understand how the different strategies used in modeling the flow influence the heat fluxes experienced by the TPS so that past predictions may be appraised and future entries in gas giant atmospheres benefit from improved understanding of different phenomena.

In the process, the capabilities of both codes have been extended. First, the numerical module responsible for computing the transport properties of the gas in SPARK has been restructured, now allowing simulation of all Solar System planets' atmospheres using the detailed Gupta/Yos transport model, by incorporating a phenomenological potential approach for unknown collision cross sections. Furthermore, the radiative transfer module in SPARK LbL has been rebuilt from scratch using Fortran Object-Oriented programming (OOP) techniques, improving efficiency of both tangent-slab and ray-tracing routines. This upgrade to both codes was found necessary so as to perform the desired sensitivity studies, while also serving as an important first step in a future integration of both numerical libraries in Fortran.

A review of past works performed regarding Galileo's entry in Jupiter is presented in Sec. II. Preflight studies in preparation for the mission are first considered, followed by subsequent attempts to reproduce the flight data with improved modeling. Section III goes into detail on the numerical models employed. Thermodynamic, kinetic, and transport models are discussed, and a comparison of Wilke/Blottner/Eucken and Gupta/Yos transport models is presented. The definition of a radiative database suitable for entry in Jupiter is analyzed, in an attempt to consider as many bound-bound, bound-free, and free-free transitions. The spectral absorption coefficient is then compared with that obtained with the HTGR code[9] for verification. The tangent-slab and ray-tracing approaches for radiative transfer are also reviewed, together with their numerical implementation. Finally, the numerical framework and results obtained for Galileo's entry are presented in Sec. IV, and final conclusions are drawn in Sec. V.

II. LITERATURE REVIEW

A. Mission preparation and flight data treatment

Two sets of ground-based experiments conducted independently have previously studied the chemical kinetics of H_2–He mixtures. In 1972, Leibowitz[10] performed electric arc driven shock tube experiments, having explored shock velocities ranging from 13 to 20 km s^{-1}. Similar experiments were conducted by Livingston and Poon[11] in 1976 for shock velocities between 26 and 46 km s^{-1}. Both studies assessed the ionization relaxation processes between atomic hydrogen and electrons in the high-temperature shock layer downstream of the shock wave, and recommended expressions for the chemical kinetic rates in agreement with the experimental measurements were provided.[12] These old experiments are still used today for the validation of theoretical models, emphasizing the value attributed to experimental ground testing.

The data collected in these experiments allowed several preflight numerical predictions to be obtained. Moss and Simmonds[13–16] performed extensive simulations during the mission preparation phase. These ranged from the Viscous Shock-Layer (VSL) to full Navier-Stokes solutions, studying the effects of distinct physicochemical processes taking place, such as turbulence, ablation, spallation, and wall reflectivity, all under the assumption of chemical equilibrium. Tiwari and Szema[17] also studied the role of thermochemical nonequilibrium and precursor heating in Galileo's entry, having found a significant increase in both convective and radiative heating compared to an equilibrium solution. The influence of precursor heating is enhanced due to nonequilibrium conditions and radiative heat fluxes at the stagnation point were found to increase by 10% when this phenomenon was modeled.

After the mission's success, the flight data regarding the heat shield temperature and ablation captured by the sensors during descent was analyzed by Milos *et al.*[2] The actual heat shield recession along the wall of the descent probe is shown in Fig. 2. Predictions obtained by other authors are also presented for comparison. Moss and Simmonds' preflight predictions highlight the classical trend observed for the Galileo mission: the nose recession was largely overpredicted, while the opposite was true in the frustum region, resulting in a nonoptimal TPS thickness distribution.

B. Numerical reproduction of flight data

Since the publication of the data gathered by Galileo, many authors have tried to numerically replicate the descent probe's heat shield recession.

Among the first to have done so, Matsuyama *et al.*[19] performed coupled radiative transfer simulations assuming thermochemical equilibrium, while assessing the influence of the tangent-slab approximation when compared to the ray-tracing approach for radiative transfer calculations. A multiband model containing just 570 important H wavelengths was employed in the spectral radiation calculation, and the ray-tracing approach was found to predict a 10% lower stagnation point radiative heating when compared to the tangent-slab formulation.

In 2005, the same authors studied the effects of turbulence coupled with ablation products injection near the wall,[18] using a modified version of the Baldwin-Lomax turbulence model proposed by Park.[20] This time, a tangent-slab analysis was conducted using 4781 wavelengths in the range 750–15 000 Å and radiative transitions from C, C_2, C_3, O, O_2, and CO were considered. It was found that turbulence-induced diffusion of ablation products in the shoulder decreased radiation absorption, leading to higher radiative heat fluxes in this region. This allowed for an improved prediction of the recession profile, as shown in Fig. 2.

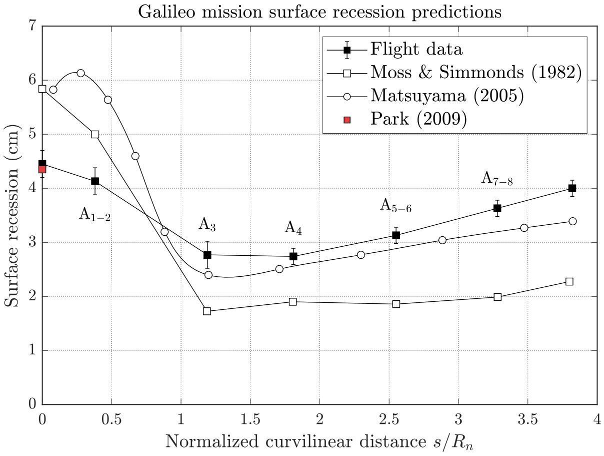

FIG. 2. Predicted heat shield recession comparison.[2,16,18]

Subsequently, Furudate *et al.*[21] studied the effects of thermochemical nonequilibrium using Euler's equations and the tangent-slab approximation for radiative transfer, while considering only H and H^+ radiation. By using an improved model for the kinetic rates of atomic hydrogen ionization proposed by Park,[22] it was found that nonequilibrium effects could reduce the predicted radiative heat fluxes in the stagnation point by as much as 10%, leading to closer agreement with flight data.

Park[23] also studied the stagnation point radiative heating under chemical equilibrium. Radiative transfer calculations were performed using 10 001 wavelengths, accounting for radiative transitions from carbonaceous species resulting from TPS ablation. Radiation blockage caused by spallation of TPS particles was also considered. The author reported good agreement with the flight data on the stagnation point recession (see Fig. 2), provided the vacuum ultraviolet (VUV) bands for C_2 and C_3 species were incorporated in the radiative analysis.

More recently, Reynier *et al.*[1,24] compiled the state-of-the-art in the modeling of gas giant atmospheres (H_2–He) for convective heating predictions and reviewed previous attempts in simulating the Galileo entry. Three distinct models differing in thermodynamic, kinetic, and transport databases were developed and compared with past estimates. The increasing level of detail provided by the improved databases, which are supported by state-to-state kinetic studies that have been conducted in recent years,[25,26] is shown to decrease the convective component of the wall heat fluxes by between 70% and 85% when compared to older estimates.

It should be noted that all previous studies taking into account the radiation field resulting from uncontaminated species, only consider radiative transitions from H and H^+ (radiative recombination processes in the case of H^+). The effect of He lines and H_2 bands, for instance, remains unaccounted for. Moreover, the true three-dimensional character of radiative transport is rarely acknowledged, and modeling of transport properties has exclusively relied on Wilke's mixing rules, despite their poor accuracy at high temperatures. Furthermore, thermochemical equilibrium has been assumed in most studies performed in the past. While thermal equilibrium may be a good approximation at lower altitudes, where the atmospheric density is sufficiently high to rapidly induce it, chemical nonequilibrium is still present throughout the flowfield. The higher altitude trajectory point focused in the present work is characterized by strong nonequilibrium for both processes. A thorough study of these effects is still lacking for understanding the unresolved mysteries regarding the Galileo entry.

III. NUMERICAL MODELS

This section is divided in two parts. First, the physical models and databases concerning the CFD simulations performed are presented. Thermodynamic, thermochemical nonequilibrium and transport models are discussed, and the Wilke/Blottner/Eucken and Gupta/Yos models for transport are compared. The second part defines the radiative database and describes the tangent-slab and ray-tracing formulations for radiative transfer, their shortcomings and implementation details.

A. Physicochemical flowfield modeling

1. SPARK CFD solver

SPARK—*Software Package for Aerothermodynamics, Radiation, and Kinetics*—is a CFD code for the simulation of hypersonic nonequilibrium flows written in Fortran 03/08. It was developed by Lopez and Lino Da Silva,[4] and is capable of solving both Euler and Navier-Stokes compressible-flow equations in 0D (temporal relaxation), 1D (postshock relaxation), or 2D geometries (planar and axisymmetric). Thermochemical nonequilibrium models are available, through multitemperature and state-to-state formulations. The CFD solver uses a finite volume method with block-structured meshes. The Harten-Yee upwind TVD scheme,[27,28] which is a second order spatial and temporal scheme based on Roe's solver, is implemented, with an extension to two dimensions using an Alternating Direction Implicit method.

2. Flowfield governing equations

In the present work, the compressible Navier-Stokes equations are used to solve for the flowfield properties around the descent probe. These conservation equations may be written as

$$\frac{\partial(\rho c_s)}{\partial t} + \nabla\cdot(\rho c_s \boldsymbol{V}) = \nabla\cdot\boldsymbol{J_s} + \dot{w}_s, \tag{1a}$$

$$\frac{\partial(\rho \boldsymbol{V})}{\partial t} + \nabla\cdot(\rho \boldsymbol{V}\otimes\boldsymbol{V}) = \nabla\cdot[\boldsymbol{\tau}] - \nabla p, \tag{1b}$$

$$\frac{\partial(\rho e)}{\partial t} + \nabla\cdot(\rho e \boldsymbol{V}) = \nabla\cdot\Big(\boldsymbol{V}\cdot[\boldsymbol{\tau}] - p\boldsymbol{V} - \boldsymbol{q}\Big), \tag{1c}$$

where c_s is the species mass fraction, ρ the mixture's density, $\boldsymbol{V}$ the velocity vector, p the pressure, e the mixture's specific internal energy, and $[\boldsymbol{\tau}]$ the viscous stress tensor. The heat-flux vector is defined without the radiative source term since an uncoupled approach was employed,

$$\boldsymbol{q} = -\sum_k k_k \nabla T_k + \sum_s \boldsymbol{J_s} h_s, \tag{1d}$$

where k_k and T_k are the thermal conductivity and temperature associated with thermal energy mode k, $\boldsymbol{J_s}$ is the mass diffusion flux vector and h_s denotes the species' specific enthalpy. Finally, the two-temperature model used (detailed in Sec. III A 5) requires an additional energy conservation equation for the nonequilibrium vibrational temperature of H_2, described through

$$\frac{\partial(\rho e_{\mathrm{v,H_2}})}{\partial t} + \nabla\cdot(\rho \boldsymbol{V} h_{\mathrm{v,H_2}}) = \nabla\cdot\Big(\boldsymbol{J}_{\mathrm{H_2}} h_{\mathrm{v,H_2}} + k_{\mathrm{v,H_2}}\nabla T_{\mathrm{v,H_2}}\Big) + \dot{\Omega}_{\mathrm{V\text{-}T}}. \tag{1e}$$

3. Thermodynamic models

A seven species mixture composed of H, He, H_2, H^+, He^+, $H_2{}^+$, and e^- was considered in the present work, similar to the one employed in several other postflight studies.[1,18,21,29] Jupiter's unperturbed atmosphere is assumed to consist of 86.4% H_2 and 13.6% He, in mole percent, corresponding to the values measured during the actual flight as reported by Milos *et al.*[2]

The thermodynamic properties of the gas are computed from the classical high-temperature results of statistical thermodynamics.[30,31] In particular, the energies associated with each species' translational, rotational, vibrational, and electronic excitation energy modes are computed using, respectively,

$$e_{\mathrm{trans},s} = \frac{3}{2}R_s T, \qquad s \in \{\mathrm{All}\}, \tag{2a}$$

$$e_{\mathrm{rot},s} = R_s T, \qquad s \in \{\mathrm{Mol.}\}, \tag{2b}$$

$$e_{\mathrm{vib},s} = \frac{h\nu_s/k_{\mathrm{B}}T}{e^{h\nu_s/k_{\mathrm{B}}T} - 1} R_s T, \qquad s \in \{\mathrm{Mol.}\}, \tag{2c}$$

$$e_{\mathrm{el},s} = R_s T^2 \frac{\partial}{\partial T}\Big(\ln Q_{\mathrm{el},s}\Big), \qquad s \notin \{\mathrm{e}^-\}, \tag{2d}$$

where R_s is the specific gas constant, k_{B} represents Boltzmann's constant, ν_s is the species' fundamental vibration frequency and Q_{el} is the electronic excitation partition function. Electronic-vibrational energy level constants for H_2 were taken from Fantz,[32] and rotational constants from the compilation of Huber and Herzberg.[33] Data for $H_2{}^+$ was also taken from Huber and Herzberg.[33] All electronic level data for atomic species was taken from NIST,[34] and the corresponding number of electronic energy levels used in the evaluation of (2d) is presented in Table I. The total internal energy of each species e_s is then obtained by summing over all individual contributions.

4. Chemical kinetics

Chemical nonequilibrium is taken into account by solving a mass conservation equation for each species separately [Eq. (1a)]. The mass source term $\dot{w}_s$ is modeled via the usual relation, expressing the net rate resulting from the forward and backward reactions,

$$\frac{\dot{w}_s}{\mathcal{M}_s} = \sum_r \Delta\nu_{sr}\left\{k_{f,r}\prod_s [X_s]^{\nu'_{sr}} - k_{b,r}\prod_s [X_s]^{\nu''_{sr}}\right\}, \tag{3}$$

where $\mathcal{M}_s$ is the species' molar mass and $\nu_{s,r}$ are stoichiometric coefficients associated with products (ν''_{sr}) and reactants (ν'_{sr}) for reaction r. The forward reaction rates $k_{f,r}$ are computed from an Arrhenius equation of the form

$$k_{f,r} = C_r T_{f,c}^{\alpha_r} \exp\left(-\frac{E_{f,r}}{k_{\mathrm{B}} T_{f,c}}\right), \tag{4}$$

where $T_{f,c}$ is the rate-controlling temperature, while the backward rates $k_{b,r}$ are calculated from the equilibrium constant for the reaction.

Several kinetic schemes regarding entry into gas giant atmospheres composed of H_2–He mixtures can be found throughout the literature.[1,10,17,21] All of them highlight the importance of properly modeling molecular hydrogen dissociation, as it is among the first processes taking place behind the shock wave.[1] The kinetic model employed in the present work is based on the rates obtained by Leibowitz and Kuo,[10] complemented with the associative ionization reaction rate for $H_2{}^+$ used by Furudate.[21,29] The reactions and corresponding constants entering Eq. (4) are presented in Table II.

A word of caution is in order at this point. Upon gathering and comparing the data available in the literature regarding the

TABLE I. Number of electronic energy levels considered per species in (2d) for both codes used in this work.

	Electronic energy levels	
Species	SPARK	SPARK line-by-line
H	157	111
H^+	1	idem
He	192	197
He^+	148	idem
H_2	$X^1\Sigma_g$, $B^1\Sigma_u^+$, $c^3\Pi_u$, $a^3\Sigma_g^+$, $C^1\Pi_u$, $E^1\Sigma_g^+$, $F^1\Sigma_g^+$, $e^3\Sigma_u^+$, $d^3\Pi_u$, $h^3\Sigma_g^+$, $K^1\Sigma_g^+$, $G^1\Sigma_g^+$, $i^3\Pi_g$, $I^1\Pi_g$, $j^3\Delta_g$, $J^1\Delta_g$, $D^1\Pi_u$, $H^1\Sigma_g^+$	idem + $B'^1\Sigma_u^+$, $g^3\Sigma_g^+$, $l^3\Pi_u$, $H\bar{H}^1\Sigma_g^+$, $o^3\Sigma_u^+$, $B'\bar{B}^1\Sigma_u^+$, $r^3\Pi_g$, $k^3\Pi_u$, $v^3\Pi_g$, $R^1\Pi_g$, $D'^1\Pi_u$, $s^3\Delta_g$, $n^3\Pi_u$, $P^1\Sigma_g^+$, $O^1\Sigma^+$, $S^1\Delta_g$, $D''^1\Sigma_u$
${H_2}^+$	$X^2\Sigma_g^+$, $B^2\Sigma_g^+$, $C^2\Pi_u$	$X^2\Sigma_g^+$

Arrhenius rate coefficients for the kinetic scheme, a discrepancy was found between the data reported by some authors. More specifically, Reynier *et al.*[1] used the coefficients employed by Tiwari and Szema[17] for reactions R6–R9, which in turn were based on the work of Leibowitz and Kuo.[10] However, the C_r coefficients for those reactions originally reported by these authors were found to be two orders of magnitude lower than those used by Tiwari and Szema (and, consequently, Reynier *et al.*). Since the original rates from Leibowitz and Kuo are the ones recommended for H_2–He mixtures,[35] they were employed in the present work for all available reactions.

5. Thermal nonequilibrium

At high altitudes, where the atmosphere is thinnest and the density is low, collisions occur less frequently and thus the relaxation toward equilibrium takes longer. This translates into a larger nonequilibrium region, reaching as much as 1 cm in the stagnation region, along with a decrease in radiative heating of around 10% in the same location when compared to an equilibrium case, according to Furudate.[21] Thus, thermal nonequilibrium effects were studied in the present work, using a two-temperature model that allows for the vibrational energy levels of H_2 to be populated according to a Boltzmann distribution at a temperature T_{v,H_2} different from the remaining thermal modes, which are assumed thermalized at T_{tr}.

Despite the attempts in considering a separate free-electron temperature, unidentified instability problems in the CFD solver prevented this refined treatment in a potential three-temperature model. Nonetheless, since the radiative transfer problem is decoupled from the flowfield in the present work, and due to the strong dependence of the radiative field on the free electrons temperature, T_{e^-} was assumed equal to T_{v,H_2} in the radiative analysis, while $T_{e^-} = T_{exc}$ is assumed by the SPARK LbL solver. Because vibrational-electronic energy exchanges tend to be significantly more efficient than translational-electronic energy exchanges, this correction should improve the approximate treatment of the free electrons temperature employed in the flowfield solution.

TABLE II. Kinetic model employed in the present work and forward rate Arrhenius coefficients entering Eq. (4).

		Arrhenius rate coefficients			
Reaction	Process	C_r (m^3/mol/s)	α_r	E_f/k_B (K)	References
R1	$H_2 + H \longleftrightarrow H + H + H$	8.347×10^{13}	−1.0	5.234×10^4	10
R2	$H_2 + He \longleftrightarrow H + H + He$	4.173×10^{12}	−1.0	5.234×10^4	10
R3	$H_2 + H_2 \longleftrightarrow H + H + H_2$	1.043×10^{13}	−1.0	5.234×10^4	10
R4	$H_2 + H^+ \longleftrightarrow H + H + H^+$	8.347×10^{13}	−1.0	5.234×10^4	10
R5	$H_2 + e^- \longleftrightarrow H + H + e^-$	8.347×10^{13}	−1.0	5.234×10^4	10
R6	$H + e^- \longleftrightarrow H^+ + e^- + e^-$	2.279×10^5	0.5	1.578×10^5	10
R7	$H + H \longleftrightarrow H^+ + e^- + H$	6.172×10^2	0.5	1.160×10^5	10
R8	$H + He \longleftrightarrow H^+ + e^- + He$	4.883×10^2	0.5	1.160×10^5	10
R9	$He + e^- \longleftrightarrow He^+ + e^- + e^-$	1.332×10^5	0.5	2.852×10^5	10
R10	${H_2}^+ + e^- \longleftrightarrow H + H$	7.076×10^8	−0.4	0.000×10^{00}	21

TABLE III. Millikan-White coefficients used in this work.[35]

Interaction	A^{MW}	B^{MW}
H_2–H	65.110	0.006 821
H_2–He	69.971	0.004 682
H_2–H_2	9.673	0.072 500
H_2–H^+	Same as H_2–H	
H_2–He^+	Same as H_2–He	
H_2–$H_2{}^+$	Same as H_2–H_2	
H_2^+–s	Same as H_2–s	

Thermal nonequilibrium requires solving Eq. (1e), which contains a vibration-translation energy exchange term $\dot{\Omega}_{\text{V-T}}$. The conventional Landau-Teller equation is employed for this term, with the vibrational relaxation times provided by the empirical Millikan-White correlation,

$$\left(\tau_{\text{vib}}^{s,c}\right)_{\text{V-T}} = e^{A_{s,c}^{\text{MW}}\left(T^{-\frac{1}{3}} - B_{s,c}^{\text{MW}}\right) - 18.42}\left(\frac{p}{101325}\right)^{-1}. \qquad (5)$$

The formulation presented by Thivet *et al.*[36] is then used to compute the global vibrational relaxation time for species s from the interspecies ones provided by Eq. (5). The Millikan-White coefficients used in the present work are presented in Table III, following the refit reported by Palmer *et al.*[35] that was obtained from joining previous relaxation times given in two complementary temperature ranges.[37–39] However, data are only provided for H_2–H, H_2–He, and H_2–H_2 interactions. Similar coefficients are assumed for the remaining secondary collisions, as indicated in Table III. This approximation should have a negligible impact on the energy-exchange modeling since charged species are not present to a significant extent.

6. Transport models

One important outcome of this work was the implementation of an updated database compatible with the improved Gupta/Yos formulation in SPARK, allowing for this transport model to be applied to atmospheres other than Earth's. The major motivators for this upgrade are detailed collision cross section (CCS) calculations published in the recent years by the Bari chemistry group for Jupiter-atmosphere species,[40] not to mention the phenomenological approach developed for Mars,[41] for which the CCS parameters are defined in terms of physical properties of the interacting species, thus circumventing the difficult process of finding interspecies CCS data. These transport properties—viscosity, thermal conductivity, and mass diffusion—are typically computed using the Wilke/Blottner/Eucken model (abbreviated to Wilke from now on), which is known to provide inaccurate results as temperatures increase beyond the onset of ionization.[42,43] The high temperatures encountered for Jupiter entries render this model unsuitable for transport properties calculations, the next best option being the Gupta/Yos model.

In the Wilke transport formulation, Wilke's mixing rules are employed to compute the mixture's viscosity and thermal conductivities from the individual species contributions.[44] These are in turn estimated from Blottner's curve fits[45] as a function of temperature, using the coefficients provided by Reynier *et al.*[1] for H_2–He mixtures. Finally, a unit Schmidt number is assumed when computing single species' thermal conductivities using Eucken's generalized relation, and a constant Lewis number of 0.39 is set for obtaining the mass diffusion coefficient.

The commonly known Gupta/Yos model[46] is based on a simplification of the Chapman-Enskog solution first proposed by Yos.[47] This simplification neglects the transfer of momentum or energy between species by collisions, a physical trait modeled in the mathematical formulation through the presence of nondiagonal terms in the first-order Chapman-Enskog determinant, leading to an overprediction of the mixture's thermal conductivity.[46] To quantify the practical implications of this approximation in the context of H_2–He mixtures, two Gupta/Yos models were developed and compared. The Gupta/Yos 1st Order model uses the simplification, embodying the conventional Gupta/Yos formulation commonly employed. The Gupta/Yos 2nd Order one uses the more accurate formulas proposed by Yos,[47] which take into account the effects of these nondiagonal terms. Both models are described in detail in the literature,[46] and their implementation is straightforward.

Either variant of the Gupta/Yos model requires knowledge of the CCSs for all possible pairs of species present in the mixture at a given time. The database implemented in SPARK and used throughout this work follows that reported by Bruno *et al.*,[40] who provide a set of curve-fit expressions and coefficients for Jupiter-atmosphere components, valid between 50 and 50 000 K. To account for resonant charge-transfer processes, a charge-exchange correction is applied to the interactions H–H^+, He–He^+, and H_2–$H_2{}^+$. However, for H–$H_2{}^+$, He–H_2, He–$H_2{}^+$, H_2–He^+, and H_2–$H_2{}^+$ interactions, no data are presented. For these, the phenomenological potential approach proposed by Pirani *et al.*[51] is implemented to evaluate the collision integrals. These interactions are compared in Fig. 3 to those published by Biolsi[49] and Sokolova[48] for temperatures ranging 1000–25 000 K, and 2000–30 000 K, respectively. Reasonable agreement is found for the H–$H_2{}^+$ and H_2–$H_2{}^+$ interactions, provided the charge-exchange correction is applied to the latter. On the other hand, He–H_2 and He–$H_2{}^+$ phenomenological interactions present significant deviations from Biolsi and Sokolova's data. The use of the approach in these cases is justified, first, for consistency (since it was the approach employed by Bruno *et al.*,[40] and was kept here to allow for later comparisons) and, most importantly, because the interacting species always coexist in negligible amounts inside the shock layer, meaning their effect on the mixture's transport properties will be negligible. The same may be said regarding the H_2–He^+ collision pair, for which no data were found for comparison. Finally, charged-species CCSs are evaluated assuming a screened Coulomb potential, adopting the expression and coefficients proposed by Wright *et al.*[52] Higher-order CCSs, required by the 2nd Order Gupta/Yos formulation, are avoided by making direct use of the curve fits for the ratio B^*.

The transport properties obtained using these three models and an equilibrium H_2–He mixture at 1 atm were compared with several sources, including: Biolsi's transport properties,[53] Reynier *et al.*'s Bari model,[1] Bruno *et al.*'s detailed calculations using a higher-order Chapman-Enskog approximation,[40,50] and a rapid calculation using NASA's CEA code.[54] Note that the composition of the atmosphere assumed by these sources varied slightly. While Biolsi's and Bruno *et al.*'s data consider $x_{H_2} = 0.89$ and $x_{\text{He}} = 0.11$ (molar fractions),

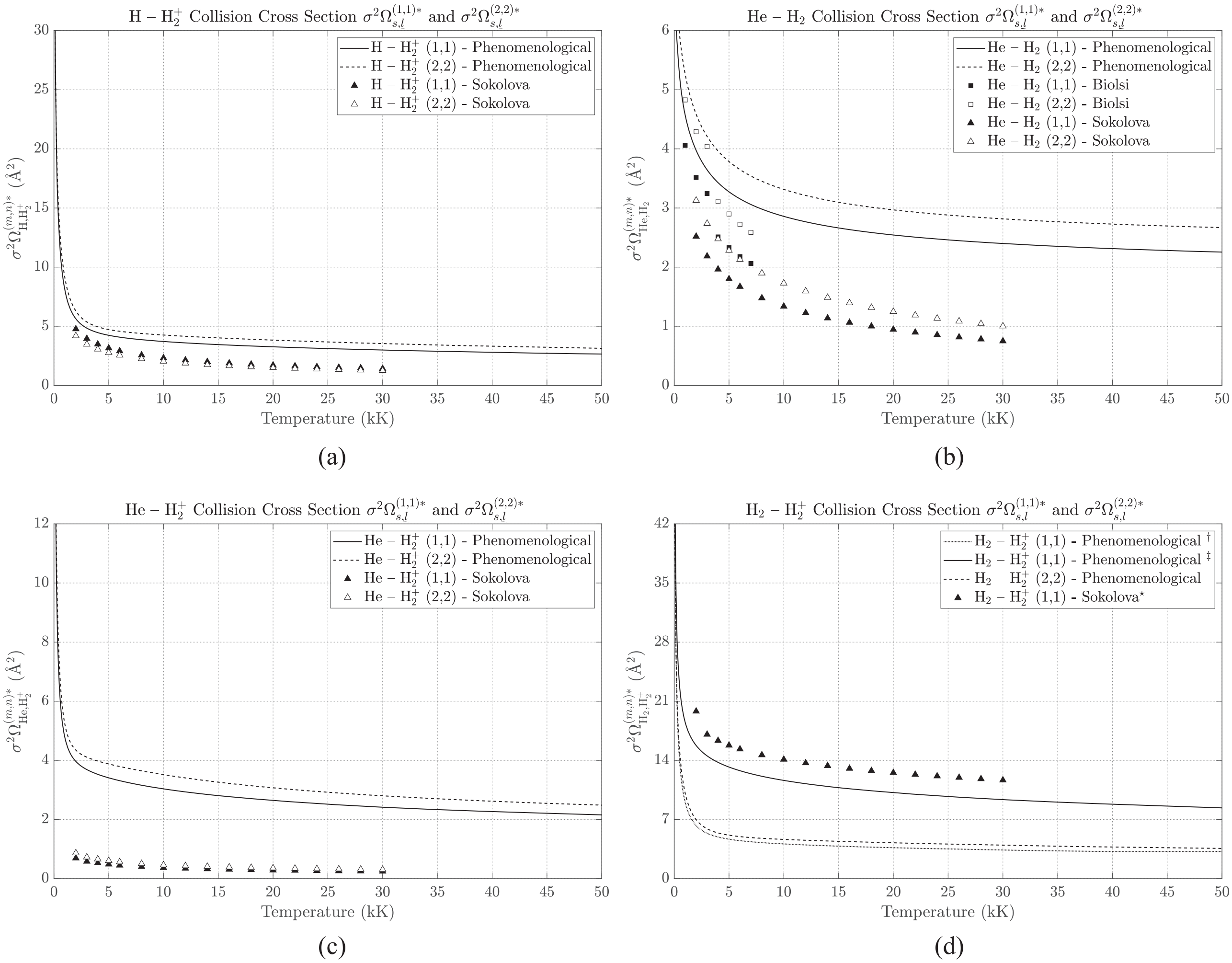

(a)

(b)

(c)

(d)

FIG. 3. Comparison of CCSs computed using the phenomenological approach with several sources.[40,48–51] (a) H–H_2^+. (b) He–H_2. (c) He–H_2^+. (d) H_2–H_2^+. † CCS before charge-exchange correction. ‡ CCS after charge-exchange correction. ⋆ No data were found regarding H_2–H_2^+ (2, 2).

Reynier *et al.*'s and CEA's data corresponds to a composition of $x_{\mathrm{H2}} = 0.864$ and $x_{\mathrm{He}} = 0.136$, similar to the one assumed in the present work. The comparison is presented in Fig. 4.

To the left, the Wilke model is seen to significantly underpredict the viscosity of the mixture between 5000 and 25 000 K. On the contrary, the Gupta/Yos 1st Order model overpredicts the viscosity by 50%–100% between 10 000 and 25 000 K. When comparing Bruno *et al.*'s data with the Gupta/Yos 2nd Order calculation, a better agreement is found between 20 000 and 25 000 K, but significant discrepancies still occur between 10 000 and 20 000 K. Differences between the Gupta/Yos 1st and 2nd Order models may reach 200% at 15 000 K, just by considering the effect of the nondiagonal terms. Among all sources, Biolsi's data are seen to provide the best agreement with Bruno *et al.*'s detailed calculations.

Regarding thermal conductivity, the Wilke model again leads to a significant underprediction above 5000 K. The large thermal conductivities obtained by Bruno *et al.* at higher temperatures are a result of considering a third-order Chapman-Enskog approximation for the electrons' translational thermal conductivity.[51] Again, the effect of considering the 2nd Order model over the 1st Order one is clearly seen. As aforementioned, the conductivity of the former model is decreased below that of the latter. However, this results in a less accurate calculation when compared to Bruno *et al.*'s data, especially above 10 000 K. The two peaks observed in the CEA calculation correspond to the onset of H_2 dissociation and H ionization, respectively, resulting from considering the reactive component of the specific heats in the calculation of internal thermal conductivity contributions, which does not enter the remaining data sets. A good agreement for mass diffusion coefficients is obtained between the Gupta/Yos models and Biolsi's calculations. However, large discrepancies are observed when compared with the Wilke model, except for He^+ and H_2^+, for which an acceptable agreement is obtained.

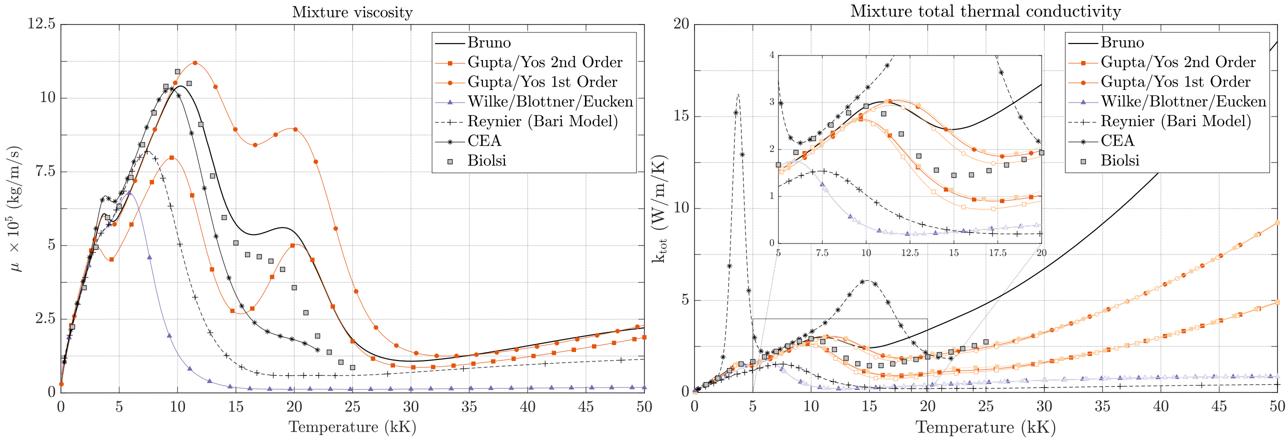

FIG. 4. Comparison of transport properties obtained from various models and literature data for equilibrium H_2–He mixture at 1 atm. The different shades of the same color on the right correspond to a calculation of the internal thermal conductivity contribution using different thermodynamic models: dark filled markers—analytic model described in Sec. III A 3, light filled markers—Capitelli coefficients, and light open markers—NASA9 coefficients.

In summary, the Wilke/Blottner/Eucken transport model confirms its inaccuracy at temperatures exceeding 5000 K, for which the Gupta/Yos model predicts significantly higher coefficients. In the present work, the Gupta/Yos 2nd Order model was adopted for simulating Galileo's entry, and the Gupta/Yos designation corresponds to the 2nd Order model from now on.

B. Radiation models

1. SPARK line-by-line radiative code

SPARK Line-by-Line (SPARK LbL), formerly known as SPARTAN, is a line-by-line radiative code maintained at Instituto de Plasmas e Fusão Nuclear[6,7] that computes the frequency-dependent emission and absorption coefficients of a gas mixture under nonequilibrium conditions. It is a libre code written in Matlab, although progress is underway toward an optimized Fortran version. While the code has been primarily developed for the simulation of low-pressure, high-temperature plasmas, characteristic of planetary atmospheric entry applications, it can also serve other applications such as combustion and low-temperature plasma radiation, using a detailed spectral database encompassing 134 different systems.

The code's numerical routines are capable of simulating bound atomic and molecular radiation with fine-structure effects (singlet, doublet, and triplet transitions, with Lambda-doubling effects). Bound-free radiation like photodissociation, photoionization, and photodetachment transitions can be accounted for according to available cross sections from the literature, regardless of whether they are cross sections integrated over specific temperature ranges, or state-specific cross sections. Free-free transitions like Bremsstrahlung are also accounted for, using the most popular theoretical and semiempirical expressions found in the literature.

The Voigt line profile routine is able to account for Doppler and Lorentz collisional broadening processes (collisional, resonance, van der Waals, and Stark). It has been specifically tailored for fast and accurate spectral simulations through the application of a variable spectral grid adaptive algorithm.[6] Calculations are fully customizable by the user, allowing compromises between accuracy and computation speed.

The code is split in two blocks: an excitation module, providing the populations of the atomic and molecular species internal levels, and a radiative module, which calculates the emission and absorption coefficients. The excitation routine currently calculates the internal levels populations considering multitemperature (T_{rot}, T_{vib}, T_{exc}) Boltzmann distributions, but may be bypassed with the direct supply of internal levels populations from an external hydrodynamic/state-to-state code.

2. Radiative database definition

The definition of a spectral database suited to the Galileo entry conditions has been carried out.

First, as the extremely high postshock temperatures lead to a highly dissociated flow, great care must be exerted in defining a detailed set of atomic transitions, encompassing bound, and continuum transitions. A considerable advantage of atomic radiation modeling is that the number of radiative transitions is moderate. Accordingly, calculation times and spectral grid sizes are kept reasonably low. Thus, the atomic spectral database accounts for as much radiative transitions as possible, regardless of their quantitative significance. For example, the contribution from bound transitions of He and He^+ may in general be neglected since the first excited states lie, respectively, 20 eV and 40 eV above the ground state. This means these will not be considerably populated for the temperature range of interest, if a Boltzmann distribution for the internal levels is assumed. Nevertheless, these radiative systems have been accounted for the sake of completeness, as they also have a negligible impact on calculation times and spectral grid sizes. All the atomic line data are issued from NIST.[34]

As the ionization degree of the flow is considerably high, great care must be exerted when modeling the broadening mechanisms for these atomic transitions, especially for what pertains to Stark broadening mechanisms. Two possibilities may be considered: either a general expression may be used, such as the one proposed by Johnston for N and O atomic transitions,[55] or a reference Full Width at Half Maximum (FWHM) for each transition may be supplied and then scaled for the electronic temperature and density of the gas.[56] Since radiation from H atomic lines is key to the overall radiative fluxes, a literature review was carried out for the FWHM measured for the different H transitions, for a range of electronic temperatures and densities. The data are then fitted to the expression (note that Stark shift is ignored in the present model):

$$\Delta\lambda_{\mathrm{SB}}(N_{\mathrm{e}^-}, T_{\mathrm{e}}) = \Delta\lambda_{\mathrm{SB},0}\left(\frac{T_{\mathrm{e}}}{10\,000}\right)^{m}\left(\frac{N_{\mathrm{e}^-}}{10^{22}}\right)^{n}, \qquad (6)$$

where $\Delta\lambda_{\mathrm{SB},0}$ is the reference Stark FWHM for the transition, T_{e} is the electron-electronic temperature, and N_{e^-} the electron number density. Whenever the m and n exponents are not supplied, $m = 2/3$ and $n = 1$ are assumed ($m = 2/3$ was found to better represent the T_{e} dependence than the value $m = 1/3$ proposed by Park for air species[55]).

The data used for the fit to Eq. (6) was retrieved from Griem[56] for the Lyman (α, β, γ, δ) and Balmer (α, β, γ, δ) transitions, Ref. 57 for the Paschen (α, β) transitions, Ref. 58 for the Paschen γ transition, Ref. 59 for the Brackett (α, β) transitions, and estimated for the Pfund α transition. The fitting parameters are presented in Table IV. From this data, a semiempirical general function for the missing transitions of hydrogenoïd species was derived, similar to the one proposed by Johnston for air species,[55]

$$\Delta\lambda_{\mathrm{SB},0} = 1.72\times 10^{-21}\times(E_{\mathrm{ion}} - E_{\mathrm{u}})^{2.5}\lambda^{1.7}n_{\mathrm{u}}^{9.3}, \qquad (7)$$

TABLE IV. Compiled $\Delta\lambda_{\mathrm{SB},0}$ Stark broadening parameters for the main transitions of atomic hydrogen.

Transition	$\Delta\lambda_{SB,0}$ (Å)	n	m
Lyman α	0.0077	0.820	−0.27
β	0.2588	0.670	0.04
γ	0.1903	0.900	−0.53
δ	0.8088	0.690	0.03
ϵ	2.4480	0.300	0.05
Balmer α	1.5549	0.810	−0.23
β	9.7473	0.670	0.03
γ	11.5227	0.870	0.00
δ	21.1192	0.680	0.06
Paschen α	23.5440	0.667	0.38
β	74.2190	0.667	0.38
γ	87.9980	0.667	0.38
Brackett α	158.7400	0.750	0.33
β	238.1100	0.750	0.33
Pfund α	0.7260	0.667	0.33

which is used whenever data are absent for specific transitions. In Eq. (7), E_{ion} is the ionization energy, E_{u} is the upper state energy, n_{u} the main quantum number of the upper state, and λ is the transition wavelength in Ångström.

Besides the atomic transitions, H_2 transitions are also considered, in an effort to determine its impact using a line-by-line approach. This molecule is present to a certain extent in the shock-layer (before dissociation) and near the wall (due to recombination processes), and thus its effects on the radiative heating may be important. The Lyman ($B^1\Sigma_u^+$–$X^1\Sigma_g^+$) and Werner ($C^1\Pi_u$–$X^1\Sigma_g^+$) VUV transitions are considered, which will be the more relevant in terms of emission, since the $B^1\Sigma_u^+$ and $C^1\Pi_u$ are the lowest excited states that may radiate toward the ground state ($X^1\Sigma_g^+$). The weaker Fulcher band ($d^3\Pi_u$ − $a^3\Sigma_g^+$) was also included in the database. Likewise, the transitions $B'^1\Sigma_u^+$–$X^1\Sigma_g^+$, $D^1\Pi_u$–$X^1\Sigma_g^+$, $B''B^1\Sigma_u^+$–$X^1\Sigma_g^+$, and $D'^1\Pi_u$–$X^1\Sigma_g^+$ are accounted for since they are connected to the ground state. Although these will be weakly emissive transitions, due to the higher-lying states $B'^1\Sigma_u^+$, $D^1\Pi_u$, $B''B^1\Sigma_u^+$, $D'^1\Pi_u$ being sparsely populated, they will be strongly absorptive, considering the opposite is true for the ground state $X^1\Sigma_g^+$.

For the $X^1\Sigma_g^+$ level energies, the data proposed by Pachucki[60] is fitted to adequate Dunham and v-dependent constants, while for the $B^1\Sigma_u^+$ and $C^1\Pi_u$ states the same procedure is applied to the levels measured by Abgrall.[61] The Dunham coefficients for the higher-lying states are retrieved from the Huber and Herzberg compilation[33] (these will be superseeded by data derived from the potential curves proposed by Fantz[32] in the future.). Finally, the transition probabilities use the data compiled by Fantz.[32]

This data set for discrete atomic and diatomic transitions has been complemented by a data set for continuum transitions (bound-free photodissociation/photoionization, and free-free Bremsstrahlung), also following an extensive literature review. Since continuum transitions typically lead to compact spectral grids, all possible transitions from all species are considered, regardless of how marginal these may be. A great majority of this data is issued from astrophysical plasma research since H and He species make up for a majority of the Universe.

Table V presents the entire spectral database considered in the scope of this work.

3. Radiation database verification

In this section, the absorption coefficients obtained with SPARK LbL's spectral database are compared with those published by Perrin *et al.*[9] using the HTGR code database. Note that SPARK LbL's database adopts significantly more radiative systems than HTGR, which considers only bound-bound H and He atomic transitions, photoionization continua for H and He, bound-bound Lyman ($B^1\Sigma_u^+$–$X^1\Sigma_g^+$) and Werner ($C^1\Pi_u$–$X^1\Sigma_g^+$) molecular bands for H_2, as well as free-free Bremsstrahlung. The comparison is performed using an equilibrium H_2–He mixture at 1 atm and initial molar composition in the ratio H_2:He = 89%:11%. The spectral absorption coefficients resulting from both databases are presented in Fig. 5 for two temperatures: 5000 K, representative of the boundary layer temperature surrounding Galileo's TPS, and 20 000 K, close to the temperatures found in the high-temperature shock layer.

The results show good agreement between the two spectral databases, although a more pronounced Stark broadening of

TABLE V. Description of spectroscopic database for H_2–He mixtures developed in the present work for SPARK LbL.

Species	Database	Model	Lines	Electronic levels	References
Atomic lines					
H	NIST	. . .	24	. . .	34
He	NIST	. . .	152	. . .	34
He^+	NIST	. . .	140	. . .	34
Atomic photoionization					
H	TOPBase	Level Q_a	. . .	55	64
He	TOPBase	Level Q_a	. . .	53	64
He^+	TOPBase	Level Q_a	. . .	55	64
Atomic photodetachment					
H^-	. . .	Global Q_a	. . .	. . .	65 and 66
He^-	. . .	Global Q_a	. . .	. . .	67
Bremsstrahlung					
H	. . .	Global Q_a	. . .	. . .	71
He	. . .	Global Q_a	. . .	. . .	74
He^+	. . .	Global Q_a	. . .	. . .	75
H_2^-	. . .	Global Q_a	. . .	. . .	76

Species	System	Upper state - lower state	Bands $(v'_{\mathrm{max}}, v''_{\mathrm{max}})$	References
Molecular band systems				
H_2	Lyman	$B^1\Sigma_u^+ - X^1\Sigma_g^+$	(10, 10)	32, 60, and 61
	Werner	$C^1\Pi_u - X^1\Sigma_g^+$	(10, 10)	32, 60, and 61
	Fulcher	$d^3\Pi_u - a^3\Sigma_g^+$	(18, 18)	32 and 62
	$B' - X$	$B'^1\Sigma_u^+ - X^1\Sigma_g^+$	(8, 10)	32, 33, and 63
	$D - X$	$D^1\Pi_u - X^1\Sigma_g^+$	(10,10)	32, 33, and 63
	$B''B - X$	$B'\bar{B}^1\Sigma_u^+ - X^1\Sigma_g^+$	(10,10)	32 and 33
	$D' - X$	$D'^1\Pi_u - X^1\Sigma_g^+$	(10,10)	32 and 33
Species	Database	Model	Lines	References
Molecular photoionization				
H_2	. . .	Global Q_a	. . .	68–70
Molecular photodissociation				
H_2	. . .	Global Q_a	. . .	72 and 73
H_2^+	. . .	Global Q_a	. . .	72

hydrogen atomic lines is observed in the HTGR database, especially at 20 000 K. As temperatures increase, the molecular absorption lines of H_2 present in the UV region are progressively overcome by atomic H Lyman absorption. At lower temperatures, as in the 5000 K case presented, these molecular absorption mechanisms are still very important. This raises the question of whether or not the assumption of neglecting H_2 radiative processes is reasonable, as has been almost exclusively done in the past. There are two regions in the flow where H_2 exists in significant amounts: near the wall, where atomic H recombination occurs, and at the shock location, just before the temperatures increase beyond the onset of dissociation. The increased emission from H_2 transitions in the shock region, counteracted by the potential increase in absorption resulting from inclusion of these mechanisms in the boundary layer, were investigated in the present work.

C. Radiative transfer modeling

The energy transfer process resulting from radiative transitions is modeled through the solution of the radiative transfer equation, which may be written in the form

$$I_\nu^{\theta,\phi}(L) = I_{\nu,0}^{\theta,\phi} e^{-\tau_\nu(L)} + \int_0^{\tau_\nu(L)} \frac{j_\nu}{\kappa_\nu} e^{-(\tau_\nu(L)-\tau_\nu)} \, \mathrm{d}\tau_\nu, \qquad (8)$$

expressing the spectral intensity of radiation as a function of the spectral coefficients j_ν, κ_ν, and optical thickness σ_ν at a position L along the line of sight specified by the direction (θ, ϕ). The radiative heating the probe experiences during entry is obtained by integrating $I_\nu^{\theta,\phi}$ over the spectral and hemispherical domain, after solving Eq. (8) for the spectral directional intensity at every location along the wall, that is,

$$q_{\mathrm{rad}} = \int_0^\infty \int_0^{2\pi} \int_0^{\pi/2} I_{\nu,\mathrm{wall}}^{\theta,\phi} \cos\theta \sin\theta \, \mathrm{d}\theta \, \mathrm{d}\phi \, \mathrm{d}\nu. \qquad (9)$$

The formulation often employed to solve Eq. (8) is the tangent-slab approximation, which is known to overpredict the radiative heating at the stagnation region by 10%–15%, whereas differences of up to 70% have been reported[77,78] for the shoulder and afterbody regions when compared to the ray-tracing approach. Both models were implemented in a radiative transfer module in Fortran and integrated with the SPARK LbL spectroscopic database. A description of both approaches for radiative transfer and their implementation details will now be presented.

1. Tangent-slab approximation

The fundamental assumption behind this approximation is that the variation of the flow properties along a line of sight normal to the body is considered to extend along an infinite slab tangent to the wall (hence the name) at any given point. Equivalently, the flow properties are considered to vary only in the direction normal to the body for the purpose of the radiative transfer computations. The concept is displayed in Fig. 6, illustrating its application to the stagnation point of a given flowfield. This approximation prevents

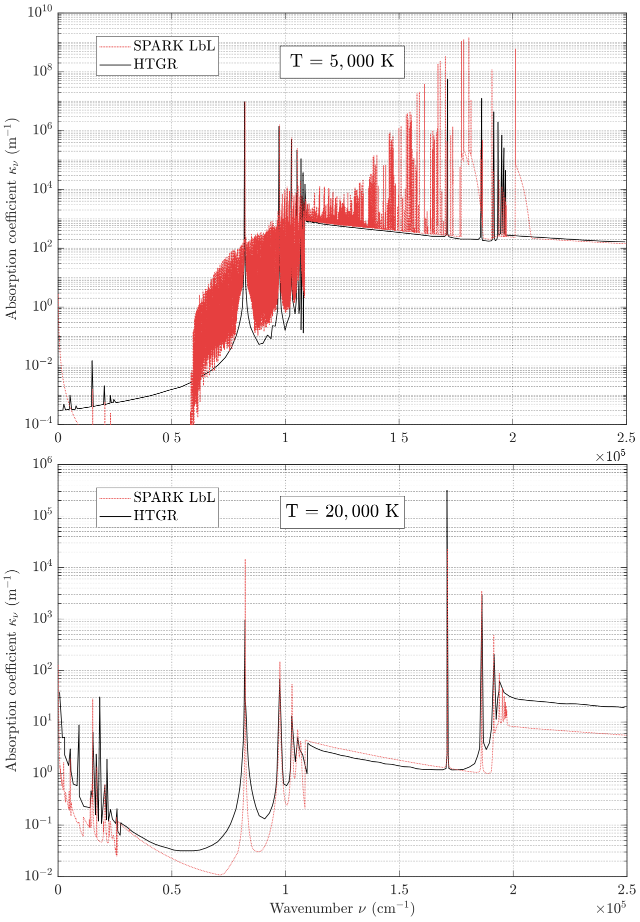

FIG. 5. Comparison of SPARK LbL and HTGR's spectral databases for H_2–He mixture at 5000 K (top) and 20 000 K (bottom). The detailed molecular absorption lines between 60 000 and 110 000 cm^{-1} could not be manually retrieved from the source,[9] although they are present in the reported HTGR results.

radiative transitions having an impact other than at the wall location directly normal to them, leading to a localized modeling of inherently nonlocal phenomena.

The tangent-slab assumption allows the evaluation of the directional integral in Eq. (8) to be performed analytically, lending a great deal of simplification to the approach when computing the radiative heating through Eq. (9). This radiative heat flux is now simply

$$q_{\text{rad}}^{\text{TS}} = 2\pi \int_0^\infty \int_0^{z_\infty} j_\nu \, \mathscr{E}_2[\tau_\nu(z)] \, \mathrm{d}z \, \mathrm{d}\nu, \tag{10}$$

where $\mathscr{E}_2(x)$ is the exponential integral of order 2, for which an approximation is provided by Johnston,[79]

$$\mathscr{E}_2(x) \approx 0.2653e^{-8.659x} + 0.7347e^{-1.624x}. \tag{11}$$

2. Ray-tracing

The ray-tracing approach is a more physically consistent method since it relies on the direct integration of Eq. (8) along a set of rays/directions. The equation is solved for every frequency by marching along a given ray between the upstream and wall boundaries to obtain the spectral intensity $I_{\nu,\text{wall}}^{\theta,\phi}$ at the vehicle's surface. The process may be easily parallelized by distributing the rays to different processor threads, as was done in the present work, and the radiative heating is then obtained from Eq. (9).

Given that several hundred rays are generally required for an accurate directional discretization of the hemisphere, each of which intersecting on the order of 100 cells in the computational domain, and that an accurate spectral resolution for emission and absorption coefficients generally requires between 10^4 and 10^5 frequency points, or even 10^6–10^7 if a detailed line-by-line method is employed, as is the case in this work, it is no surprise that preference is given to the computationally friendly tangent-slab approximation. This is accentuated when flowfield-radiation coupling is considered since in this case the rays must cover the whole spherical domain at every point in the flowfield, not just the ones at the wall. However, Johnston and Mazaheri[80] have shown that a coupled tangent-slab solution may be used in conjunction with a final ray-tracing iteration to provide radiative heating values within 1% accuracy in coupled flowfield-radiation simulations. In the present work, the flowfield and radiation are treated in an uncoupled approach.

At the heart of the ray-tracing model is the directional discretization of the hemispherical domain providing the directions (θ, ϕ) along which Eq. (8) is solved. A simple approach that is often (inadequately) implemented is to select a set of constant $\Delta\phi$ and $\Delta\theta$ values and subdivide the domain into equally spaced intervals, resulting in a cluster of rays near the poles, as can be observed in Fig. 7(a). The alternative technique implemented in the present work relies on the so-called Fibonacci Lattice, which distributes points along a tightly wound generative spiral contained on the surface of the sphere.[81] The lattice points are generated as follows. Letting

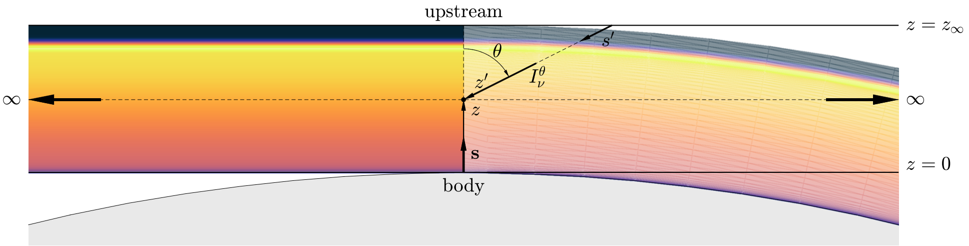

FIG. 6. Tangent-slab approximation. The two-dimensional flowfield profile (right) is approximated at a point by transferring the variation along the normal to that point into a slab tangent to the wall that extends to infinity (left).

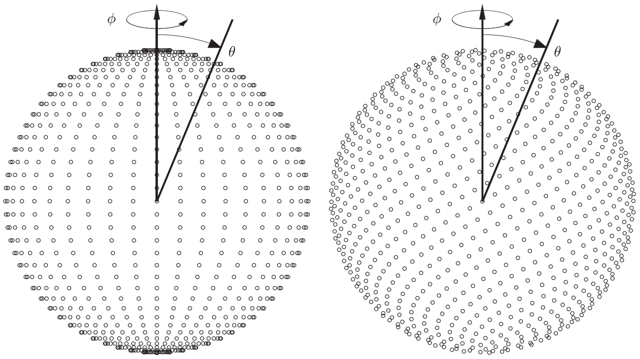

(a) (b)

FIG. 7. Different approaches for directional discretization compared. (a) Constant $(\Delta\theta, \Delta\phi)$. (b) Fibonacci Lattice.

i range from $-N_{\mathrm{FL}}$ to N_{FL}, where N_{FL} is any natural number, the spherical coordinates of the ith point are given in radians by

$$\begin{cases} \theta^{(i)} = \dfrac{\pi}{2} - \arcsin\left(\dfrac{2i}{2N_{\mathrm{FL}}+1}\right), \\ \phi^{(i)} = 2\pi i\left(\tilde{\phi}\right)^{-1}, \end{cases} \tag{12}$$

where $\tilde{\phi}$ is the golden ratio, defined as $\tilde{\phi} = \frac{(1+\sqrt{5})}{2}$. The spherical sampling of points using the Fibonacci Lattice is presented in Fig. 7(b), where the two approaches with 737 rays are compared. The improved uniformity provided by this distribution is evident when compared to the constant $(\Delta\theta, \Delta\phi)$ grid.

When considering axisymmetric flows, the inherently three-dimensional ray-tracing radiative transfer problem may be solved in just two dimensions by taking advantage of their symmetric nature. Specifically, one should exploit the fact that any point (x, y, z) in the domain may be traced back to an equivalent point $(x, \bar{y}, 0)$ with the same flow properties.[82] Letting x be the symmetry axis, this mapping is encoded in the transformation

$$\begin{cases} x_{2\mathrm{D}} = x_{3\mathrm{D}}, \\ \bar{y}_{2\mathrm{D}} = \sqrt{y_{3\mathrm{D}}^2 + z_{3\mathrm{D}}^2}. \end{cases} \tag{13}$$

Once the directional discretization is set up and the trajectories of the rays through the flowfield are known, the emission and absorption coefficients must be found along each line of sight. These depend on the flowfield temperatures and number densities, which are only defined on the CFD grid cell-centers. Thus, the accuracy of the radiative transfer algorithm will be subject to the way the cell-centered CFD solution is used by the radiative solver. The current option available in SPARK LbL is to feed the cell-centered temperatures and species' number densities to the radiative solver, which then outputs the corresponding spectral coefficients defined at the cell-centers. However, in general the rays' trajectories along which the spectral coefficients need to be found will not coincide with the grid cell-centers, meaning an approximate treatment must typically be employed.

The simplest option is to consider the emission and absorption coefficients to be constant along a given cell, inheriting the spectral values of the cell-center. However, this may potentially introduce large spatial integration errors in locations where the mesh is coarse, or if the integration is carried out over lengthy rays, in which case the error accumulates with each cell. Another option is to assume a linear variation of the spectral coefficients between cells. This assumption for the absorption coefficient would result in an integral that cannot be evaluated analytically, leading to a costly numerical integration. The alternative suggested and implemented by Johnston and Mazaheri[80] is to consider a linear variation for the emission coefficient and a constant value for the absorption coefficient. Both options were implemented and compared in this work, and will now be briefly described.

a. Constant coefficient approach. Here, the radiative transfer equation is solved by marching along a given ray through the cells it intersects and solving the equation

$$I_p^{out} = I_p^{in} e^{-\kappa_\nu^{(i,j)} L_p} + \frac{j_\nu^{(i,j)}}{\kappa_\nu^{(i,j)}}\left[1 - e^{-\kappa_\nu^{(i,j)} L_p}\right] \tag{14}$$

in a cell-by-cell philosophy, where I_p^{in} and I_p^{out} are the radiative intensities entering and leaving a given intersected cell, L_p is the length of the intersection with cell (i, j), and p is simply an index representing the cell intersection number for the given ray. The marching procedure starts at the upstream boundary with $I_1^{in} = 0$ and Eq. (14) is computed iteratively using the relation $I_p^{in} = I_{p-1}^{out}$ until the algorithm arrives at the wall.

b. Linear interpolation approach. Referring to Fig. 8, each ray is subdivided in segments, each delimited by interpolation points spread along the ray. These are the midpoints of the intersection between the ray's trajectory and the computational grid and are labeled s_p according to the intersection number, where s is the distance traveled along the ray between the wall and the upstream boundary. Two additional interpolation points are defined at the ray

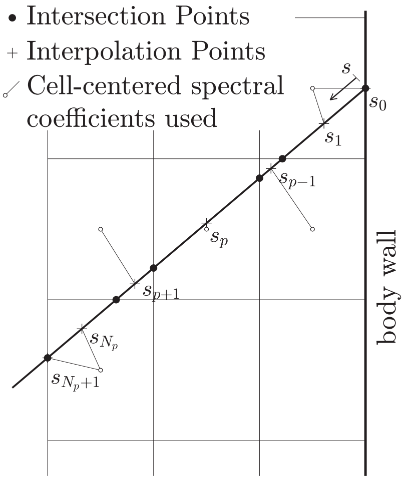

FIG. 8. Numerical implementation of the linear ray-tracing interpolation approach.

extremities, namely, s_0 and s_{N_p+1}, and the linear interpolation is performed between the interpolation points along a given ray. Hence, the spectral coefficients must be defined at each of these locations. Since these are only defined at the cell-centers, it was assumed that the spectral coefficients at a given interpolation point are equal to their value at the cell-center they belong to, as represented by the connections in Fig. 8.

With these assumptions, the radiative intensity of a given ray reaching the wall, $I_\nu(s_0)$, is equal to

$$\begin{aligned} I_\nu(s_0) &= I_\nu(s_{\max})e^{-\tau_\nu(s_{\max})} \\ &\quad + \sum_{p=0}^{p_{\max}-1} \frac{a_p}{c_p^2}\Big[(c_p s_p + 1)e^{-\tau_\nu(s_p)} - (c_p s_{p+1} + 1)e^{-\tau_\nu(s_{p+1})}\Big] \\ &\quad + \sum_{p=0}^{p_{\max}-1} \frac{b_p}{c_p}\Big[e^{-\tau_\nu(s_p)} - e^{-\tau_\nu(s_{p+1})}\Big], \end{aligned} \tag{15}$$

where the coefficients a_p, b_p, and c_p are defined in Ref. 80.

Regardless of the option chosen for the spatial integration of the radiative transfer equation, the final step in obtaining the surface radiative heating is the directional integration over the hemisphere, as defined by Eq. (9), followed by an integration over the spectral domain. Regarding the directional integration, a typical integration quadrature cannot be employed since the directional grid constructed from the Fibonacci lattice is irregular in θ and ϕ. This complication can be avoided by using a Monte-Carlo-based integration technique, which is justified by the small number of variables and the large number of rays (samples). The spectral radiative heating at a given location at the wall is then simply

$$q_\nu = 2\pi \frac{1}{N_{\text{rays}}} \sum_{r=1}^{N_{\text{rays}}} I_{\nu,r} \cos\theta_r, \tag{16}$$

where N_{rays} represents the total number of rays considered for a given wall point, and θ_r is the angle between the ray and the wall normal. The resulting q_ν is then integrated over the frequency spectrum to yield the surface radiative heating.

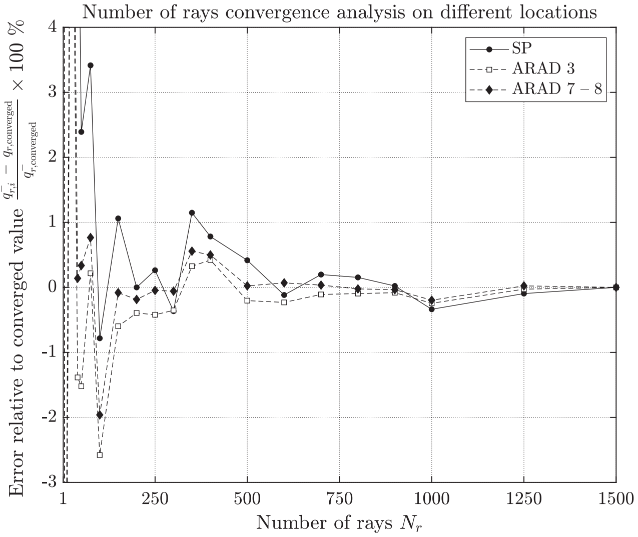

FIG. 9. Directional discretization convergence analysis at three different locations along the body.

The ray-tracing approach implemented in this work has been validated in the past. Predictions for the Exomars entry[83] were found to produce the same results as an independent ray-tracing calculation.[84] Nonetheless, the convergence of the improved directional discretization implemented in this work is assessed by computing the radiative heat fluxes at three different locations along the body (namely, the stagnation point, ARAD 3 and ARAD 7–8—both shown in Fig. 10) using (16) with an increasing number of rays. The results are presented in Fig. 9. Although significant fluctuations occur at lower levels of directional discretization, the results show surprisingly good levels of accuracy at a relatively low number of rays (just 50 rays are sufficient to keep the accuracy to within 5% of the value computed using 1500 rays).

IV. RESULTS AND DISCUSSION

This work focuses on the trajectory point of Galileo at 180 km altitude, where strong nonequilibrium conditions are expected due to the low density atmosphere. Reynier *et al.* recently studied the convective heat fluxes at this trajectory point under nonequilibrium conditions,[1] allowing for qualitative comparisons to be drawn. Table VI presents the flowfield test matrix simulated in the present work. The influence of the two transport models (Wilke and Gupta/Yos) described previously is assessed in both thermal equilibrium and nonequilibrium conditions (1T and 2T), assuming an axisymmetric laminar flow with no angle of attack.

All simulations assume an isothermal, noncatalytic wall at 3000 K, conditions similar to those used by Reynier *et al.*[1] Wall catalycity effects are expected to be overshadowed by the intense ablation products injection near the wall, and thus, its effects should be unimportant. Assuming a wall temperature of 4000 K did not show a significant influence on the flowfield, according to Reynier.[24] The thermodynamic, kinetic, and energy-exchange models described previously were applied, and whenever thermal nonequilibrium was considered (2T cases in Table VI), the modified Park rate-controlling temperature model is applied to the forward rate for the dissociation reactions of H_2, using an exponent of 0.7.

The computational domain surrounding the Galileo probe is illustrated in Fig. 10. Two ARAD sensors, representative of mid-body and near-shoulder regions, are also displayed. Sensitivity studies presented later were conducted at these locations, together with the stagnation point. The mesh was refined at strong-gradient

TABLE VI. Test matrix used in the present work.[1,2]

Case	Alt. (km)	Time (s)	V (m s^{-1})	T (K)	p (Pa)
Wilke 1T	180	42.06	46 674	161.9	27.5
Wilke 2T					
Gupta/Yos 1T					
Gupta/Yos 2T					

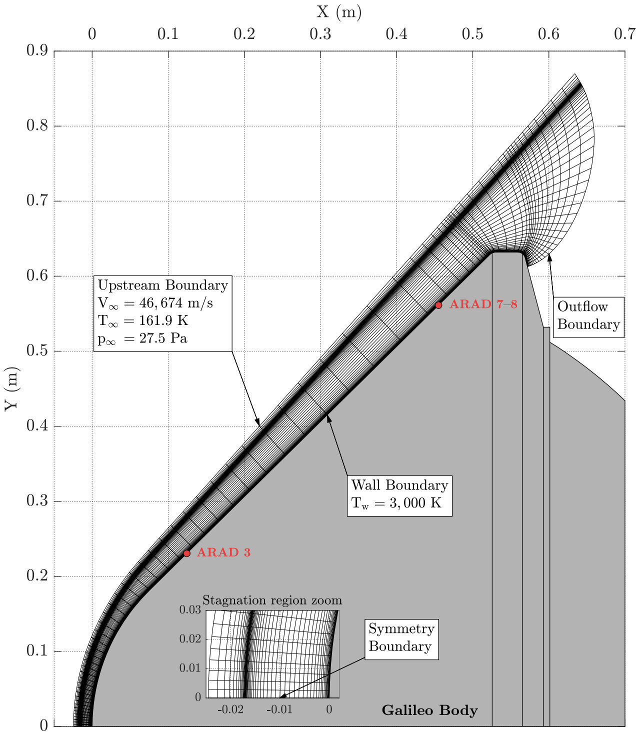

FIG. 10. Computational mesh used in CFD simulations.

regions and extended beyond the strong expansion issuing from the shoulder. This extension was necessary so as to properly treat ray-tracing computations near this region; otherwise, the computational domain would not be defined for part of the hemispherical domain at this location. However, this introduced significant challenges to the simulation of the flow, as the large expansion would reduce the pressure to near-vacuum values, and the solution therefore easily destabilized, despite the implicit scheme used for temporal discretization. A suggested workaround was given to the author by Markus Fertig at the 8th International Workshop on Radiation of High Temperature Gases. If the sonic line reattaches to the body before the shoulder [as is the case here—see Fig. 12(a)], the shoulder expansion does not require modeling if one only cares for the forebody solution, and the conical region may simply be extended with no impact on the forebody flowfield. Unfortunately, there was no time to follow the suggestion in the present work, despite having the potential to solve part of the stability issues faced.

On top of this, the extreme velocity and very small Courant–Friedrichs–Lewy numbers required to stabilize the numerical scheme (dynamically adjusted from 10^{-4}–10^{-2} at the start to 10^{-1} closer to convergence), meant that very small time steps were used [$\mathcal{O}(10^{-12}\text{s})$], and convergence took a long time. Furthermore, the time marching procedure toward steady-state could not handle a starting condition at 46 674 m s^{-1}. As a result, the strategy developed for allowing the solution to evolve was: start the simulation initially at 2 km s^{-1}, then let the shock detach from the surface and relax to a distance from the wall; then, increase the velocity to 10 km s^{-1} and allow for subsequent relaxation; finally, increase the velocity to its final value of 46.674 km s^{-1} until steady-state (convergence) is attained.

A. Flowfield and convective heating

The computational grid was established on the basis of a mesh convergence study performed on a 1T model flowfield. A total of four meshes were studied in terms of convective, radiative, and total heat fluxes on the surface of the probe. The stagnation line temperatures were also followed closely, providing both local and global criteria for the convergence of the solution. The results of this study are presented in Fig. 11, where the radiative heating was obtained using the ray-tracing approach. Clearly, there is not much gain in increasing the number of cells in the direction normal to the surface above 60. As a result, a 72 × 60 mesh was used throughout this work.

General features of the 2T Gupta/Yos flowfield around Galileo at the 180 km altitude trajectory point are presented in Fig. 12. At the left, the Mach number contours near the stagnation region are shown. The subsonic flow rapidly accelerates to supersonic speeds along the spherical portion of the domain, and the sonic line attaches back to the body close to the start of the conical section of the probe. The flow is then mostly supersonic, except in the small region of the boundary layer near the wall, where viscous effects dominate. Figure 12(b) shows the temperature field over the probe. The flow reaches a maximum temperature above 28 000 K at the stagnation line, near the shock. The refined mesh is able to capture the boundary layer gradients, and the predicted shock standoff distance is about 1.7 cm, 13% higher than the 1.5 cm predicted by Reynier[1] at the same trajectory point.

The mole fraction fields of H and e$^-$ are displayed in Figs. 12(c) and 12(d). While atomic hydrogen is the biggest source of radiative heating experienced by the probe's TPS, the electron allows a direct assessment of the degree of ionization in the flow. Since the chemical composition is mainly governed by the kinetic model employed,

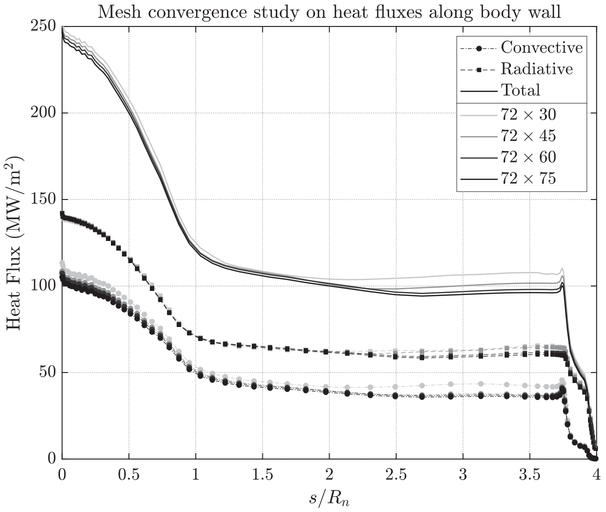

FIG. 11. Mesh convergence study performed on the convective, radiative, and total heat fluxes impacting the wall.

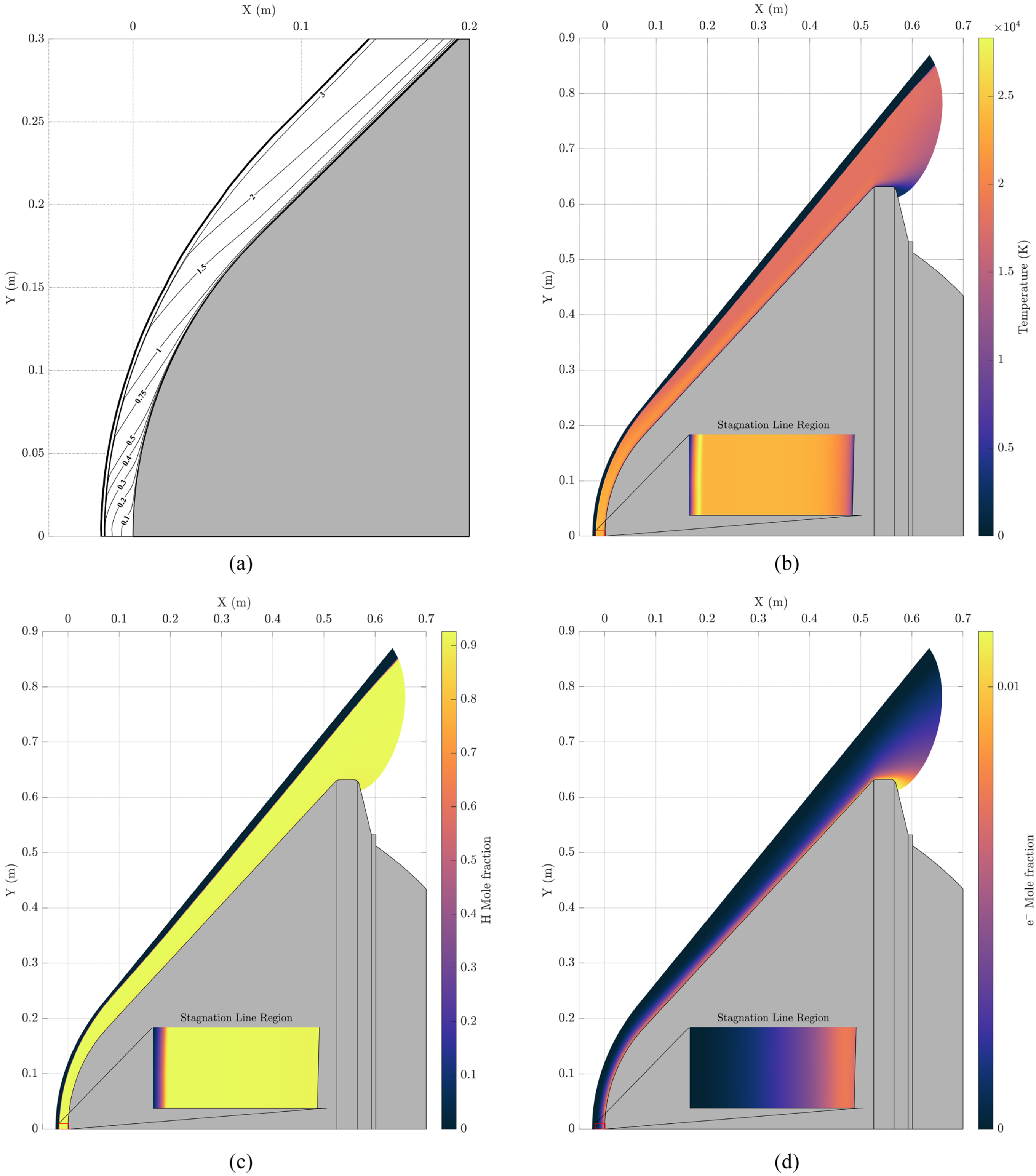

FIG. 12. Flowfield features of 180 km altitude trajectory point. (a) Mach number contours. (b) Temperature field (Gupta/Yos 2T). (c) H mole fraction field. (d) e^- mole fraction fields.

both transport models produce similar results. Atomic hydrogen is the main species present in the shock layer, resulting from rapid H_2 dissociation after the shock, making up for more than 90% of the mixture's chemical composition. Electrons reach a maximum of about 1.1% in the rapid expansion after the shoulder, as a result of H ionization. In addition, electron mole fractions increase toward the wall as the avalanche promoted by ionization reactions builds up. With no wall catalycity, recombination is not enforced at the wall, and thus, electron mole fractions do not decrease in this region. The maximum H mole fraction agrees with that predicted by Reynier *et al.*[1] However, due to the different kinetic rates employed, stronger ionization levels are predicted by the author toward the boundary layer, reaching a maximum electron mole fraction of 0.28. This is mostly a result of H ionization, and thus, the H mole fraction decreases toward the boundary layer, as opposed to that presented in Fig. 12(c).

Figure 13 presents the stagnation line temperatures obtained for the four flowfields considered, as well as a comparison with Reynier *et al.*'s results.[1] Regarding the Gupta/Yos cases, a 6% higher temperature peak is observed when thermal nonequilibrium is considered. Moreover, the nonequilibrium region extends for 3–4 mm after the shock, a value four times larger than the maximum of 1 mm predicted by Park,[23] where Leibowitz and Kuo's rates were used to estimate the nonequilibrium thickness for the Galileo case throughout its trajectory. Despite this apparently small thickness, it will be important when considering radiation from H_2, as will be discussed in Sec. IV B. After the two temperatures thermalize, the remaining shock layer is essentially in thermal equilibrium, and both 1T and 2T solutions agree. Regarding the Wilke case, similar considerations apply between the 1T and 2T cases. Reynier *et al.*'s temperature profiles significantly differ from the ones obtained in the present work. However, the differing kinetic rates mentioned in Sec. III A 4 are not the sole cause of the discrepancies. The rates employed by Reynier *et al.* were used in a separate Wilke 2T case (not presented here) and the disagreement persisted. Thus, the most likely explanation is the use of different thermodynamic databases by both codes.

When comparing both transport models, several observations should be pointed out. First, the Wilke model predicts a peak temperature about 5% higher than Gupta/Yos. Additionally, the shock is thinner and energy does not diffuse upstream to the extent observed in the latter, as revealed by the upstream temperature-increase delay between the two cases. This is a result of the larger thermal conductivity predicted by the more accurate model, allowing energy conduction at a faster rate away from the shock. As expected, the temperatures in the plateau are consistent among all cases considered. When it comes to the boundary layer in the Wilke cases, a difficulty was encountered. A temperature gap occurs at the wall and the boundary layer gradient is not perfectly captured. This issue had previously been encountered by Reynier *et al.* and is simply a result of insufficient mesh refinement near the wall. However, the mesh that the author had to consider for obtaining a smooth near-wall flow resolution had a first-cell height of just 20 nm, which is too low for our solver to handle in a realistic time frame, since the time step required to keep such a solution stable would be too small. Not even the increased mesh refinement provided by considering 90 cells normal to the wall in the Wilke cases was able to correctly predict the boundary layer gradients.

As a result of this inaccuracy, the convective heat fluxes presented in Fig. 14 for the Wilke cases are underpredicted. Here, s/R_n represents the curvilinear distance along the body normalized by the nose-sphere radius. A good agreement is found between the Gupta/Yos cases and Reynier *et al.*'s prediction in the conical body section. However, in the spherical section following the stagnation point, the Gupta/Yos convective heat fluxes are larger by up to a factor of two. Again, different thermodynamic databases or the kinetic rates employed by the author could lead to these discrepancies. Regardless of the transport model employed, thermal nonequilibrium does not appear to have an impact over the equilibrium

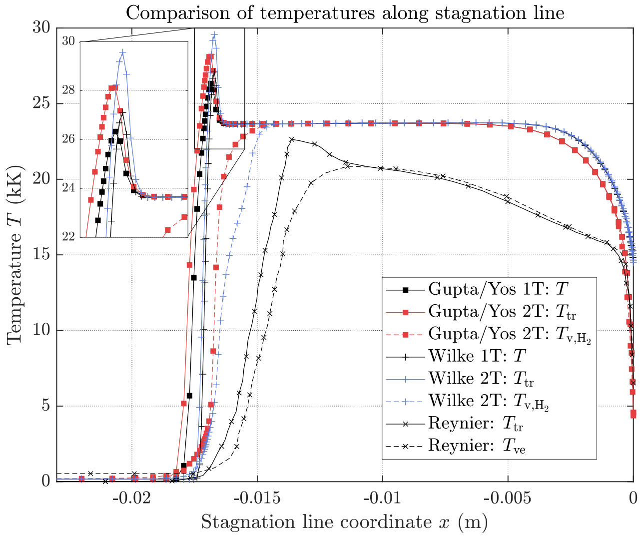

FIG. 13. Stagnation line temperature comparison.

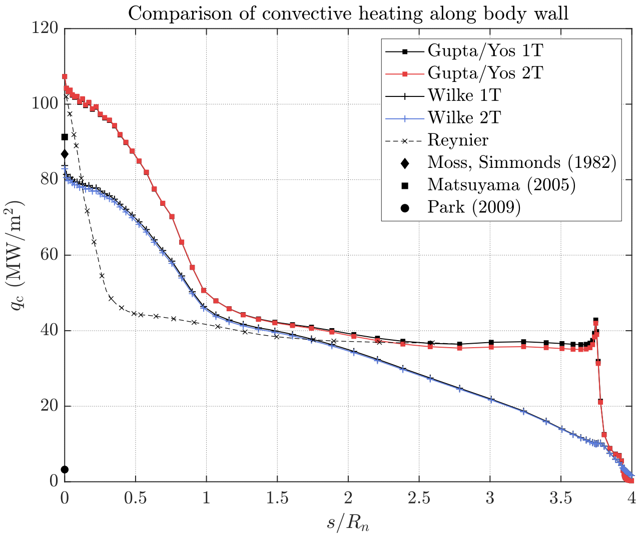

FIG. 14. Convective heat fluxes compared.

prediction. Finally, the local peak in convective heating observed near the shoulder is a result of the rapid expansion that, through the favorable pressure gradient that forms, reduces the boundary layer thickness across the shoulder curve, leading to larger temperature gradients and thus enhancing the heat transfer to the surface in this region. This increase contributes to slightly higher TPS ablation in the shoulder corner, the lowest-thickness region after entry (with just 1 cm spare of TPS material), and may have played a non-negligible role in the recession experienced at this location. The convective heating at the stagnation point agrees reasonably well with the predictions of Moss and Simmonds[16] and Matsuyama.[18] The value reported by Park is significantly lower,[23] presumably due to a combination of simplified models for the flowfield solution: VSL equations, the Wilke's transport model, and a thermochemical equilibrium assumption.

B. Radiative heating and sensitivity studies

In this section, several sensitivity studies are presented in an attempt to assess the influence of different phenomena on the radiative heating experienced by the Galileo probe, one of the major uncertainties behind this historical event. The purpose here is not to attempt a good approximation to the actual heating environment encountered during flight, as that would require a flowfield solution coupled both to radiative and material-response solvers capable of accurately predicting the ablation of the TPS material.

TABLE VII. Summary of heat flux results obtained in the present work.

Case	Assess the influence of	Convective heat fluxes (MW m^{-2})/(%[a])			Radiative heat fluxes (MW m^{-2})/(%[a])		
		SP	ARAD 3	ARAD 7–8	SP	ARAD 3	ARAD 7–8
Gupta/Yos 2T RT All	(Baseline)	107.3/. . .	43.0/. . .	35.3/. . .	115.3/. . .	53.7/. . .	49.7/. . .
Wilke 1T RT All	Transport model	83.7/—22.0	40.8/—5.1	14.0/— 60.3	174.1/+51.0	83.0/+54.6	110.9/+123
Wilke 2T RT All	Transport model	84.0/—21.7	40.9/—4.9	9.4/— 73.4	144.6/+25.4	69.0/+28.5	102.4/+106
Gupta/Yos 1T RT All	Nonequilibrium	107.3/0.0	43.1/—0.2	36.6/+3.7	142.0/+23.2	66.7/+24.2	60.9/+22.5
Gupta/Yos 2T RT H-Only	He + H_2 radiation	. . ./. . .	. . ./. . .	. . ./. . .	105.2/—8.7	52.3/—2.6	48.5/—2.4
Gupta/Yos 2T TS All	3D radiative transfer	. . ./. . .	. . ./. . .	. . ./. . .	120.2/+4.3	56.5/+5.2	51.6/+3.8
Gupta/Yos 2T RT linear interp.	Spatial integration approximation	. . ./. . .	. . ./. . .	. . ./. . .	111.7/—3.1	52.4/—2.4	48.6/—2.2
Gupta/Yos 2T TS All + Pre.	Precursor heating	. . ./. . .	. . ./. . .	. . ./. . .	355.6/+208	. . ./. . .	. . ./. . .
Gupta/Yos 2T TS All + Ab.	Ablation products	Park's systems, unchanged temperatures Park's systems, at 3000 K All systems, unchanged temperatures All systems, at 3000 K			851.9/+639 69.1/—40.1 890.7/+673 69.6/—39.6	. . ./. . .	. . ./. . .
Gupta/Yos 2T TS All + Pre. + Ab.[b]	Precursor heating ablation products	. . ./. . .	. . ./. . .	. . ./. . .	154.1/+33.7	. . ./. . .	. . ./. . .
Gupta/Yos 2T RT All + T-W	Radiative cooling	. . ./. . .	. . ./. . .	. . ./. . .	73.2/—36.5	40.2/—25.1	37.7/—24.1
Gupta/Yos 2T + T-W TS All + Pre. + Ab.[b]	Precursor heating Ablation products Radiative cooling	. . ./. . .	. . ./. . .	. . ./. . .	90.4/—21.6	. . ./. . .	. . ./. . .

All: All radiative systems considered; H-Only: Only transitions from H are considered in the radiative analysis;
RT: Ray-tracing; TS: Tangent-slab; Pre.: Precursor heating; Ab.: Ablation products; T-W: Tauber-Wakefield correction.

[a] This value corresponds to a percentage error relative to the Gupta/Yos 2T RT All case.

[b] Ablation products were considered using all systems at 3000 K.

Instead, the aim is to understand the impact that different phenomena neglected in the past have in the radiative field so that the assumptions used in previous predictions may be appraised. This way, future missions to Jupiter may benefit from a TPS design that is informed from improved preflight predictions. As the results of each sensitivity study are discussed, they can be readily compared in Table VII (available at the end of the chapter), which summarizes all the predictions obtained in the present work.

1. Transport model and nonequilibrium

The radiative heating impacting the probe depends on the transport model by virtue of the different number density and temperature fields obtained. Figure 15 shows how the number densities predicted with each model compare along the stagnation line. Apart from small differences at the shock and boundary layer regions, the two are consistent. The observed discrepancies may be explained by the increased thermal conductivity and mass diffusivity of the Gupta/Yos model at the shock, and the inability to capture the boundary layer gradients with the Wilke model, respectively.

Both transport models are compared in terms of radiative heating along the body in Fig. 16, using the conventional ray-tracing approach. Clearly, the overpredicted heat fluxes obtained with the Wilke model are consistent with the difficulty encountered at the boundary layer. The larger radiative heating is presumably a consequence of the unrealistically high temperatures obtained near the wall. However, the larger shock temperatures predicted by this model (due to the lower thermal conductivity) also contribute to the discrepancy observed between Wilke and Gupta/Yos formulations. Thus, it is difficult to conclude whether the overprediction is a result of the poor mesh refinement or a manifestation of the inaccuracy of the former model at high temperatures. Nonetheless, the 20%–25% higher heat fluxes observed with the Wilke model at the stagnation point are in agreement with the 5% higher temperature peak at the stagnation line (since emission scales with the fourth power of temperature, a 5% temperature increase may result in 20% higher radiative heat fluxes). Moreover, the results obtained with the Wilke transport model show a continuous increase in radiative heating toward the shoulder, as opposed to the slow decline predicted by the Gupta/Yos transport model. It is interesting to note that this trend conforms with the higher shoulder heat fluxes identified during postflight data treatment, despite the inaccuracies of the model at higher temperatures. This suggests that the increased radiative heating at the shoulder is a result of physical phenomena currently being neglected, such as flowfield-radiation coupling, ablation products injection or precursor heating effects.

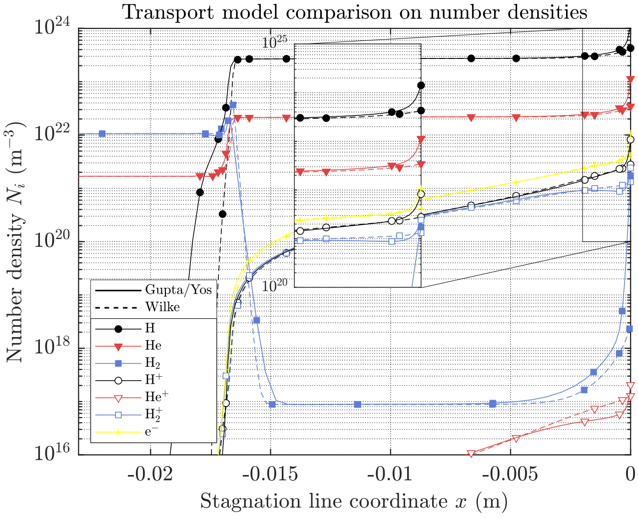

FIG. 15. Stagnation line number density comparison.

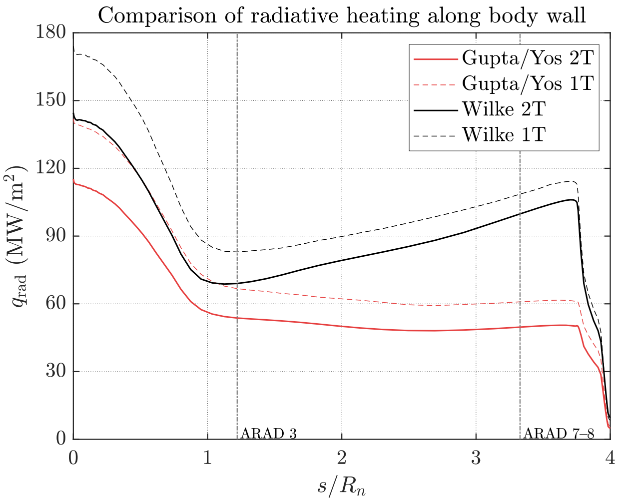

FIG. 16. Radiative heating along wall comparing all cases considered.

Figure 16 also shows that the radiative heating is overpredicted by about 20%–25% when equilibrium is assumed. The reason for this has to do with excess emission from H_2 systems arising from the shock location. This will be analyzed in more detail in Sec. IV B 2. The discrepancy is more pronounced at the stagnation point than at the shoulder, as a result of the higher temperatures. Finally, similar values are obtained for convective and radiative heating along the body in the Gupta/Yos 2T case, indicating both contributions are equally as important at 180 km altitude.

2. He and H_2 radiation

One of the main goals of the present work is to assess the influence of previously neglected radiative systems, namely, those resulting from He, He^+, and H_2 excitation/de-excitation processes.

However, the effect of each individual system is difficult to quantify. By comparing the radiative heat fluxes that result from considering a set of systems to that resulting from a different set, one is able to effectively assess the impact of the systems not shared among the two sets, provided they have systems in common. This strategy was employed in the present work, and the results are presented in Fig. 17. The tangent-slab approach was used at three different locations along the body, under thermal equilibrium and nonequilibrium conditions. Moving from the second to the last column, left to right, the radiative systems presented below are added to the analysis. For example, the second column considers only H, the third column adds He and He^+ (so, H, He, and He^+ are considered),

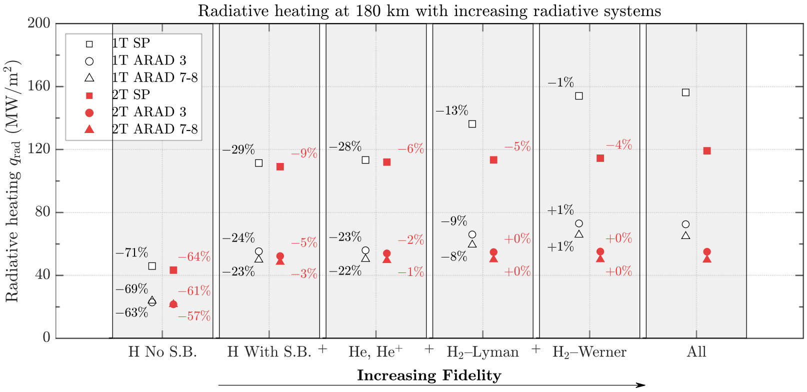

FIG. 17. Analysis on the influence of different systems on the radiative heating.

and so on. The last column corresponds to all systems, and the first one considers only atomic hydrogen transitions, while neglecting the Stark broadening (S.B.) of atomic lines. The percentages indicate the difference relative to the baseline, which corresponds to the prediction considering all radiative systems (the last column includes the contributions of continuum, Fulcher and Rydberg H_2 systems).

Clearly, Stark broadening of atomic H lines has a significant impact on the radiative heating experienced by the probe, as would be expected in such a highly ionized flow. The intense H lines are smeared, reducing the peak emission and absorption coefficients. The latter results in less self-absorption by the specific transition, significantly increasing wall heat fluxes. As a consequence, Stark broadening accounts for about 55% and 40% of the heat fluxes under thermal nonequilibrium and equilibrium conditions, respectively.

When thermal equilibrium is considered (1T case), molecular hydrogen is seen to account for 22%–28% of the total radiative heating at different locations along the body. Moreover, this contribution predominantly results from the H_2–Lyman system, although H_2–Werner is equally as important at the stagnation point. The effect of including other H_2 radiative systems is negligible, with less than 1% difference when compared to the baseline, as are the contributions due to He and He^+ systems. However, nonequilibrium conditions tell a different story. The 2T case shows a maximum difference of 9% between the radiative heating predicted with only H systems and that when considering all systems. This difference is primarily caused by inclusion of He and He^+ systems, as well as those added in the last column resulting from H_2, particularly at the stagnation point. In summary, the results point to a small increase in radiative heating due to He, He^+, and H_2 systems under thermal nonequilibrium conditions.

To further investigate the source of H_2 radiation, the spectral emission coefficient at the stagnation point was mapped against the normal distance to the wall, using the 2T solution. This allows a direct interpretation for where in the spectrum and along the stagnation line most of the radiative emission occurs. The results are presented in Fig. 18, where the bright spots correlate with stronger emission. The spectral transmittance of the shock layer to this radiation at the wall is also shown in white, calculated using $T_{\tilde{\nu}} = \exp\left(-\int_0^{z_\infty} \kappa_{\tilde{\nu}}(z)\,\mathrm{d}z\right)$. This coefficient is a measure of the spectral radiation reaching the surface, with values closer to 1 indicating low absorption.

Figure 18(a) shows the spectral emission map when considering only radiation from H systems. Atomic hydrogen emits significantly throughout the stagnation line, but the strong atomic lines are also highly absorbing, and the transmittance at these spectral locations is close to zero. However, it rapidly increases away from the peaks, leading to the strong impact of Stark broadening aforementioned. Below, Fig. 18(b) presents the same emission map when all systems are considered. There is an evident emission peak at the shock due to molecular hydrogen systems. More importantly, the remaining shock layer does not present any reabsorbing mechanisms capable of preventing this radiation from reaching the wall, especially between 1250 Å and 1700 Å. The presence of H_2 near the wall does not appear to noticeably increase absorption in this region (else, reabsorption near the wall would reduce the spectral transmittance in the spectral range mentioned before). At the lower end of the spectrum, between 700 Å and 800 Å, Fig. 18(b) indicates the presence of a strong continuum contribution, later identified to result from radiative H_2 recombination.

The spectral contributions to the radiative heating are further analyzed in Fig. 19, displaying the spectral heat flux at the stagnation point and at ARAD 7–8, using the conventional ray-tracing approach on the Gupta/Yos 2T solution. A comparison between the spectral fluxes obtained when considering only H systems and that resulting from all systems is presented, together with the cumulative heat flux after integration. An 8.7% increase in radiative heating when accounting for all systems is observed at the stagnation point, a difference that decreases to only about 2.3% at ARAD 7–8. This results essentially from the large H_2 photorecombination contribution emitted at the shock, resulting from the inverse H_2 photoionization process. A 1%–2% share may still be attributed to H_2–Lyman and H_2–Werner bands. Overall, the strong atomic H lines are responsible for most of the radiation reaching the probe's surface in both locations, as indicated by the pronounced increase in the cumulative results when an atomic line is integrated.

In summary, atomic hydrogen is the preeminent chemical species to consider for radiation, as other authors had previously assumed. Yet, they had also assumed thermal equilibrium conditions, which, when combined with inclusion of H_2 systems, is seen to greatly increase the radiative heating due to strong emission at the shock. Only when the temperature nonequilibrium induced by the

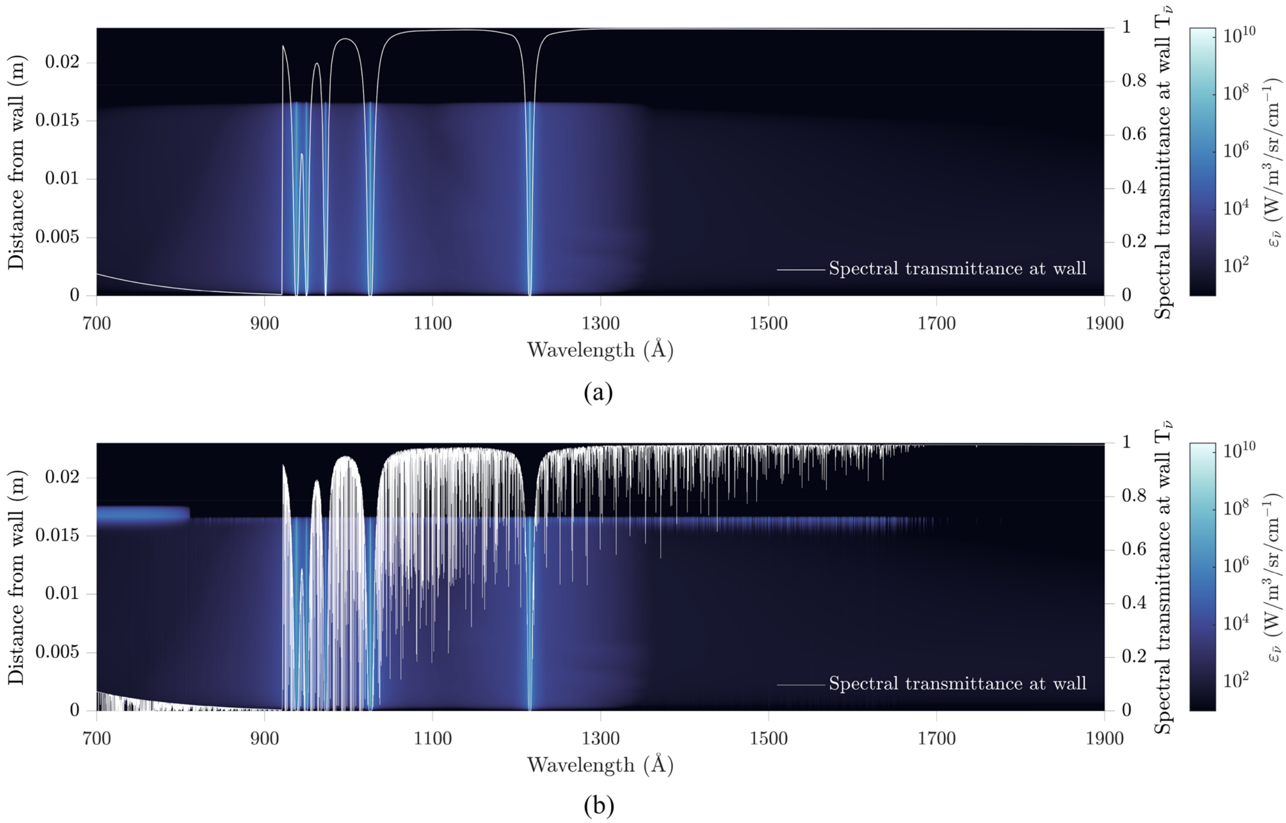

(a)

(b)

FIG. 18. Spectral emission maps along the stagnation line in the VUV region of the spectrum, where H_2 systems are active, with spectral transmittance superimposed. (a) Only H systems are considered. (b) All systems considered.

relaxation of the vibrational energy states of H_2 toward equilibrium is taken into account, does the emission lower to values similar to the ones predicted under thermal equilibrium conditions. Nevertheless, an 8.7% increase in radiative heating at the stagnation point may be attributed to inclusion of He, He^+, and H_2 systems, as indicated in Table VII.

3. Three-dimensional radiative transfer

The influence of considering different models for radiative transfer through the flowfield is analyzed in this section. Figure 20 shows the hemispherical maps of radiation intensity and heat fluxes at the stagnation point and ARAD 7–8, where a comparison between the tangent-slab and ray-tracing results is presented. The two directional quantities are related through $q^{\theta,\phi} = I^{\theta,\phi} \cos\theta$, where θ is the angle between a given direction and that normal to the wall. The $\cos\theta$ term has a filtering effect on the directional variation of the radiative intensities $I^{\theta,\phi}$, that is, the heat fluxes $q^{\theta,\phi}$ are only affected by spatial variations in $I^{\theta,\phi}$ to the extent allowed by this term. If these variations occur near the local zenith ($\cos\theta \to 1$), they are inherited by $q^{\theta,\phi}$, but if they occur at the periphery of the hemisphere ($\cos\theta \to 0$), their presence in $q^{\theta,\phi}$ is hardly noticeable. This is evident in Fig. 20. At both the stagnation point and ARAD 7–8, the differences in $I^{\theta,\phi}$ between the ray-tracing and tangent-slab approaches are more apparent at the periphery, where $\cos\theta \to 0$. In turn, this leads to a good agreement between the two approaches regarding $q^{\theta,\phi}$, which is ultimately responsible for radiative heating. At ARAD 7–8, the ray-tracing approach is able of capturing a stronger intensity from rays originating at the hottest region of the shock layer (as indicated by the circular inset), corresponding to the strong normal shock at the stagnation line, but its effect on $q^{\theta,\phi}$ is inconsequential. Due to the small shock layer thickness, the variations in flowfield properties around $\theta \sim 0°$ are small, and the tangent-slab approach is seen to provide a good approximation.

Interestingly, the stagnation point results in Fig. 20 reveal that the strongest intensity rays reaching the surface emerge from the periphery of the hemispherical domain and not from the hottest region directly normal to the stagnation point. Although counterintuitive, this results from a longer diagonal spatial integration path when $\theta \neq 0$, in which case the ray crosses a larger emitting portion of the shock. Obviously, the flowfield that follows is also absorbing radiation, but what Fig. 20 indicates is that this balance tends to favor emission over absorption, eventually leading to stronger radiative intensity.

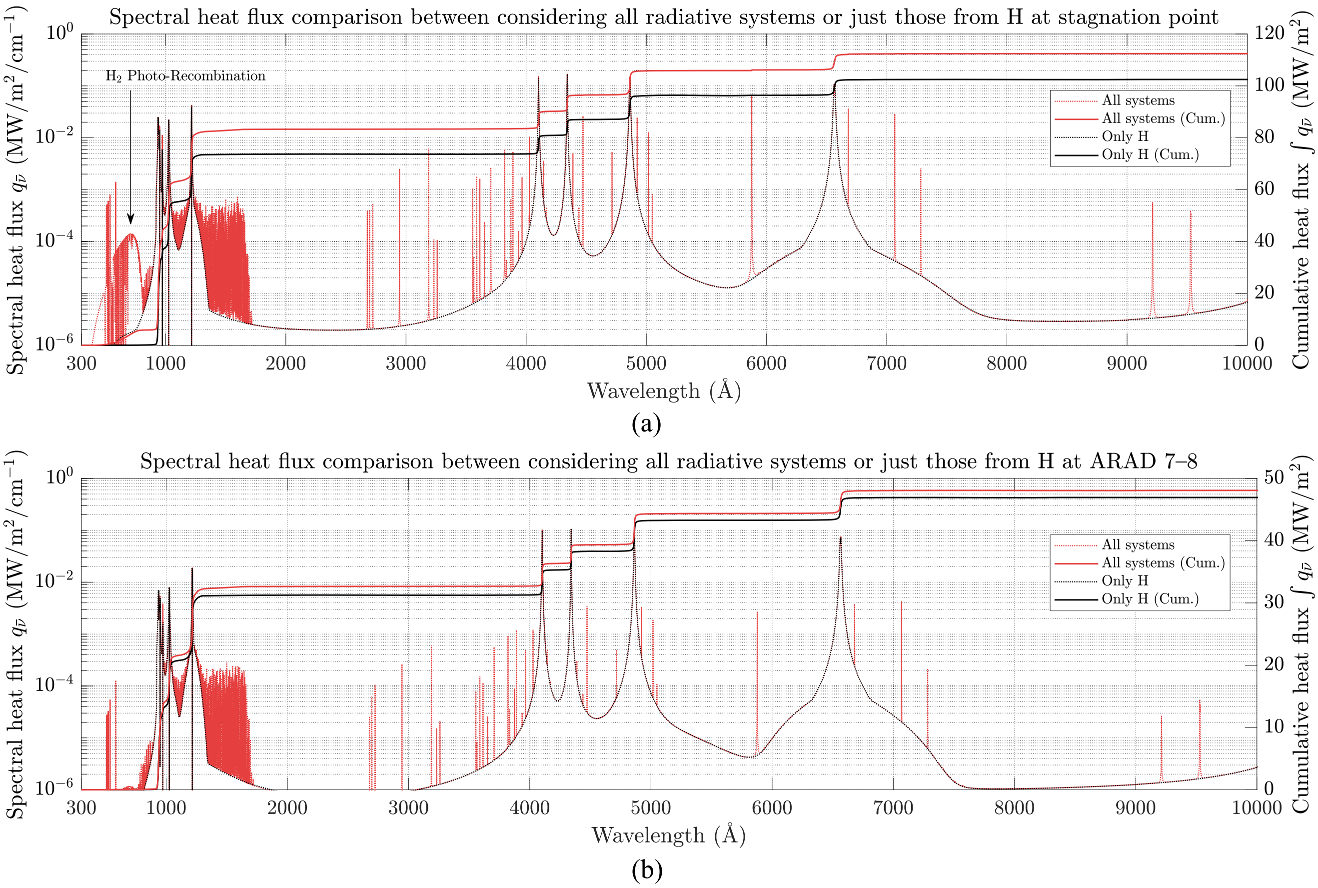

FIG. 19. Spectral radiative heating comparison when considering all systems or just those from atomic H. (a) Stagnation point spectral radiative heat flux. (b) ARAD 7–8 spectral radiative heat flux.

The good agreement between the two radiative transfer models is further supported by comparing the radiative heat fluxes along the body, as displayed in Fig. 21. The tangent-slab approach overpredicts the heat fluxes by about 3%–10% when compared to the conventional ray-tracing, a difference that increases to about 6%–12% when the comparison is performed against the more accurate linear interpolation ray-tracing model. A small discrepancy of around 3% between the two ray-tracing approaches is observed throughout the body wall. This is negligible given the fact that the linear interpolation approach takes twice the time of the conventional one. The tangent-slab model provides a very good initial estimate at a low computational cost when compared with the ray-tracing approach—a 10 min simulation in contrast to a 1 day long one, when using the conventional ray-tracing model with 500 rays.

Using the tangent-slab model, additional sensitivity studies were performed based on stagnation line results published in the literature. Given the good agreement between the two models, the conclusions gathered for this simpler case should also apply to the ray-tracing model. These will be discussed next.

4. Influence of precursor heating at the stagnation point

For strongly radiating flowfields, the influence of radiation extends beyond the shock layer. While pressure waves travel through the flow at the local speed of sound relative to it and cannot propagate upstream when it is supersonic, radiation in the form of electromagnetic waves propagates at the speed of light, and is thus able to affect the upstream flowfield. In particular, radiative absorption mechanisms in the precursor region eventually lead to photoionization and photodissociation, altering the chemical composition of the free-stream flow upstream of the shock. Additionally, several radiative transitions that do not lead to dissociation or ionization may occur, instead contributing to the excitation of the internal energy states of these particles.[85] In the context of a multitemperature approach, this results in an increase in the internal temperatures modeling the nonequilibrium behavior.

The effects of precursor heating have been studied in preparation for the Galileo mission by Tiwari and Szema.[17] Results for the stagnation point under nonequilibrium conditions showed that

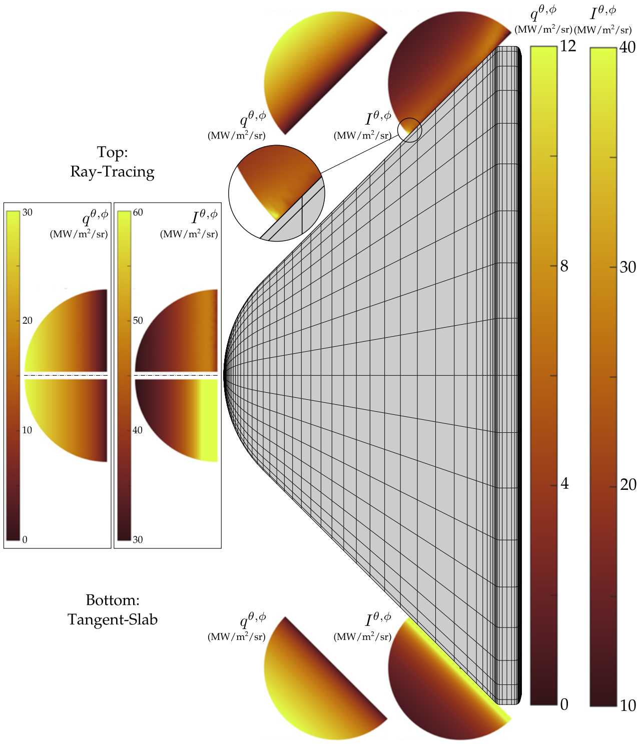

FIG. 20. Map of directional radiative intensity and heat fluxes with tangent-slab and ray-tracing approaches compared.

precursor heating would amount to 15% hydrogen becoming dissociated before even reaching the shock. Similarly, precursor photoionization was responsible for 0.8% H_2^+ in the same region. When compared to simulations where radiation to the precursor region is not modeled, both the translational and internal temperatures inside the shock layer increased by about 1%. The results reported by Johnston *et al.*[85] for a Mars-return case further support this figure. Although it may seem insignificant, note that radiation scales with the fourth power of temperature, and Tiwari *et al.* reported a 10.5% increase in radiative heat flux at the stagnation region due to these combined effects. In the precursor region, radiative absorption promotes the excitation of the internal energy levels of the particles in the upstream, thus increasing its internal temperature in the context of a multitemperature approach. At this altitude, density is too low for effective translational-internal energy exchanges to occur, and thus the translational temperature of the flow remains the same.

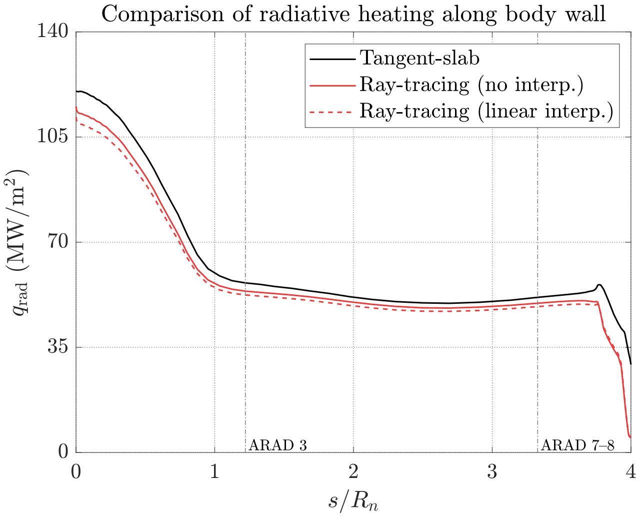

FIG. 21. Radiative heating along wall comparing all cases considered.

To estimate the impact of precursor heating at the stagnation point, in the context of the improved models applied in the present work to the Galileo case, its effects were superimposed to the Gupta/Yos 2T solution at the stagnation line. The corrections performed were as follows. Mass fractions of H_2, H, H_2^+, and e^- were corrected at the upstream to approach the values reported by Tiwari *et al.* at the shock, using the following functional form, valid for $s > s_{\mathrm{shock}}$:

$$c_i(s) = c_{i,\infty}\left[1 - \left(1 - \frac{c_{i,\mathrm{shock}}}{c_{i,\infty}}\right)e^{-k(s - s_{\mathrm{shock}})}\right], \tag{17}$$

where $i \in \{\mathrm{H}, \mathrm{H_2}^+, \mathrm{e}^-\}$, s is the distance normal to the wall along the stagnation line, $c_{i,\infty}$ is the species mass fraction at the unperturbed atmosphere, $c_{i,\mathrm{shock}}$ is the value reported by Tiwari *et al.* at the shock location, and k is a parameter adjusting the exponential variation approaching the shock. The resulting mass fraction for H_2 was set to keep $\sum c_j = 1$ across all species. To transition from this profile to the one actually computed by SPARK in the shock layer, a gluing function is applied for $s_{\mathrm{shock}} - 2\Delta s < s < s_{\mathrm{shock}}$ in the form $c_i = (1-a)c_{i,\mathrm{shock}} + a c_i^{\mathrm{SPARK}}$, where $a = (s_{\mathrm{shock}} - s)/2\Delta s$ so that no discontinuities occur since the profile used in the shock layer is the one obtained in SPARK (that is, $c_i = c_i^{\mathrm{SPARK}}$ for $s < s_{\mathrm{shock}} - 2\Delta s$). The parameter Δs was tailored to ensure a smooth transition. Regarding the temperatures, a similar process was used to increase $T_{\mathrm{v,H_2}}$ in the upstream. Finally, both temperatures were increased by 1% in the shock layer, so as to simulate the increased values reported by other authors.

The mass fractions of H, H_2, H_2^+, and e^- resulting from this approximate treatment are presented in Fig. 22(a), where a comparison is made with those before the corrections are applied. The corrected mass fractions now account for photodissociation and photoionization in the precursor region, through the processes

$$\mathrm{H_2} + h\nu \rightleftharpoons 2\,\mathrm{H}, \tag{18}$$

$$\mathrm{H_2} + h\nu \rightleftharpoons \mathrm{H_2^+} + \mathrm{e}^-, \tag{19}$$

which lead to an increase in H, H_2^+, and e^- mass fractions at the expense of H_2. Figure 22(b) presents the temperature corrections applied at the stagnation line, following the results reported by other authors on the temperature effects of precursor heating. Note that although $T_{\mathrm{v,H_2}}$ now starts increasing farther from the shock, leading to a corresponding increase in H_2 emission as previously discussed, the number density of H_2 is also significantly reduced, leading to an opposing effect. These stagnation line profiles were then fed to

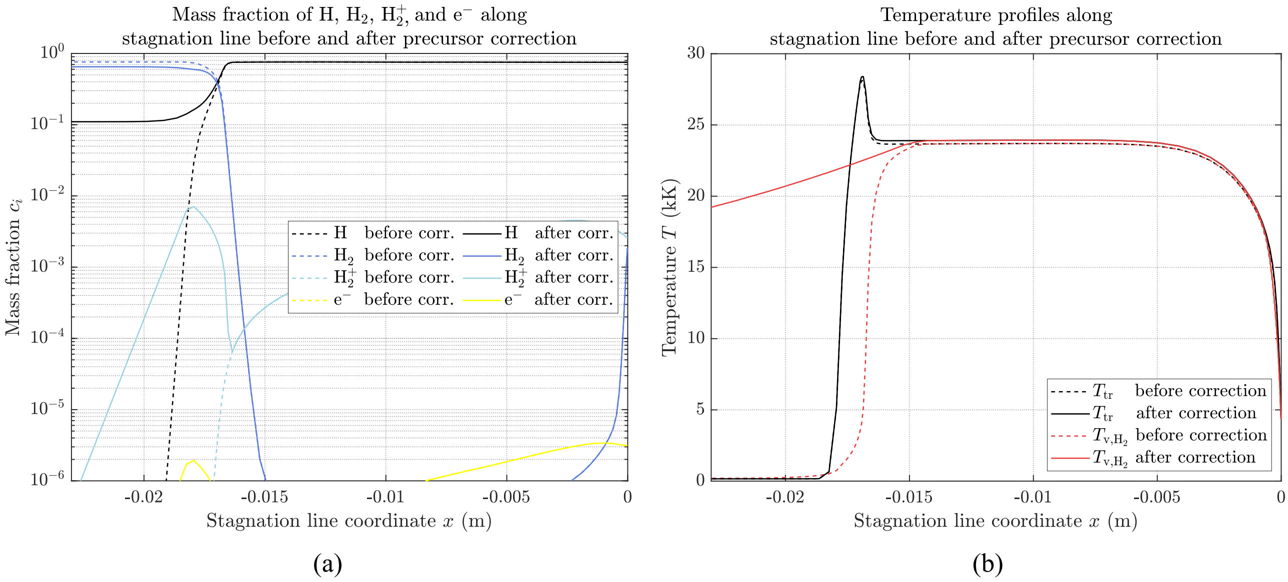

(a) (b)

FIG. 22. Stagnation line profiles before and after correction to account for precursor heating effects. (a) Mass fraction profiles. (b) Temperature profiles.

the SPARK LbL radiative solver, and the radiative heating at the stagnation point was obtained using the tangent-slab approach (a ray-tracing approach would require these corrections to be applied throughout the flowfield, resulting in a significant extrapolation of the results reported in the literature for the stagnation line).

To isolate the effects of precursor heating corrections, the spectral radiative heating obtained is compared to the one using the original tangent-slab model. The results revealed by Fig. 23 are consistent with the discussion presented earlier regarding H_2 radiation originating from the high-temperature shock. As expected, the increased vibrational temperature of H_2 in the precursor region promotes de-excitation processes before dissociation takes place at the shock, resulting in a significant increase in the contribution of H_2 to the radiative heating reaching the wall. The total heat flux accounting for the precursor heating corrections is 355.6 MW m^{-2}, nearly a 196% increase relative to the original tangent-slab value. This is a much more pronounced increase compared to the 10.5% predicted by Tiwari and Szema.[17] This discrepancy is explained by their simplified treatment of H2 radiation, which lacked the ability to consider its detailed line-by-line behavior. The thick lines in Fig. 23 show that the corrected heat fluxes start diverging from the original ones as the spectral region where H_2 systems are active is integrated, indicating that most of the observed increase is due to the correction performed on the precursor vibrational temperature of H_2, rather than the 1% temperature increase imposed inside the shock layer. In fact, if the correction to T_{v,H_2} in the precursor region is removed, the increase in radiative heat fluxes is just 3%, thus confirming this observation. This result has implications

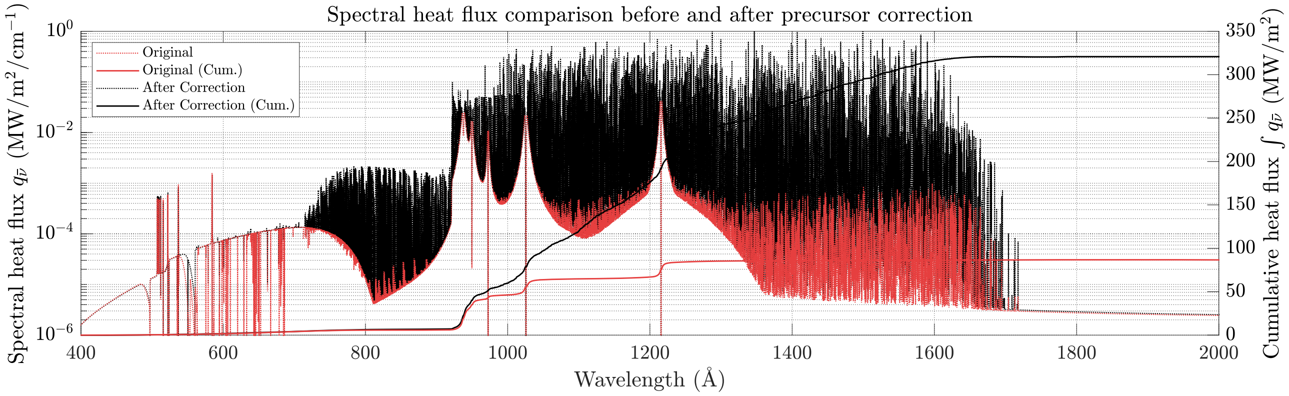

FIG. 23. Influence of precursor effects in spectral heat flux between 400 Å and 2000 Å.

in regards to the assumed Boltzmann distributions for the internal energy levels. If H_2 radiation from the shock were negligible, the shock layer would behave as an optically thick medium, and most of the radiation reaching the surface would come from the boundary layer, where thermal equilibrium conditions are safe to assume. However, if the medium is optically thin to precursor H_2 radiation, where large thermal nonequilibrium conditions exist, the Boltzmann approximation may not be reasonable. Future studies on the effect of non-Boltzmann distributions in the precursor region are necessary to fully assess the opacity of the shock layer to this radiation.

The analysis performed for precursor H_2 radiation reveals that it may have had a fundamental impact on the radiative heating experienced by Galileo, contrary to what has been assumed thus far. It also emphasizes the role of H_2 radiation in future entries to gas giants, if precursor heating is significant.

5. Ablation products injection at the stagnation point

The effects of ablation products injection in the stagnation line boundary layer are investigated in this section. An approximate treatment is performed based on the work of Park,[23] who studied ablation and spallation of C, C^+, C_2, and C_3 in the stagnation region and its effects on the stagnation point radiative heating. The aim here is to understand the extent of radiative absorption in the ablation layer due to the presence of these contaminating species, while considering the important role of H_2 radiation. More notably, the C_3 molecule is known to be a strong absorber in the VUV range, due to the Swings and VUV bands between 1200 Å and 5500 Å. Additionally, photoionization continua for C_2 and C_3 below 1100 Å have been identified by Park to significantly reduce stagnation point heat fluxes.[23] In Park's work, C_2 and C_3 radiative transitions are treated in an approximate way through temperature-dependent global absorption cross sections. The same approach was employed here concerning C_3 transitions, using the same data as Park. However, for C_2 transitions a detailed line-by-line model was used. Transitions extending from the VUV to the visible range are considered, unlike Park who only accounts for VUV transitions and the C_2 Swan bands.

Regarding non-VUV transitions, the spectral data set from Lino da Silva[86,87] already available in the SPARK LbL code was adopted. As for the VUV region, Park considers eight C_2 radiative systems in the VUV region, from which only three are reported observed in the literature,[88] namely, the Herzberg-F ($F^1\Pi_u - X^1\Sigma_g^+$), Herzberg-g ($g^3\Delta_g - a^3\Pi_u^+$) and Herzberg-f ($f^3\Sigma_g^- - a^3\Pi_u^+$) systems. Accordingly, only these three VUV transitions for C_2 have been considered here. Spectroscopic constants for the higher-lying states are issued from Huber and Herzberg,[33] whereas for lower states, the compilation from Lino da Silva[6,86] was adopted. Potential curves were refitted and the relevant vibrational wave functions were used alongside a constant electronic transition moment, estimated resorting to the data from Bruna[89] to yield the appropriate Einstein coefficients (see Ref. 86, pp. 74 for a detailed description of this approach with the corresponding equations). The temperatures in the boundary layer are still high enough to promote emission over absorption of some radiative systems, as may be the case of the C_2 Swan band in the visible range. Thus, although strong absorption in the VUV region may lead to reducing the impact of H and H_2 radiation, emission in other parts of the spectrum has the potential to neutralize this effect.

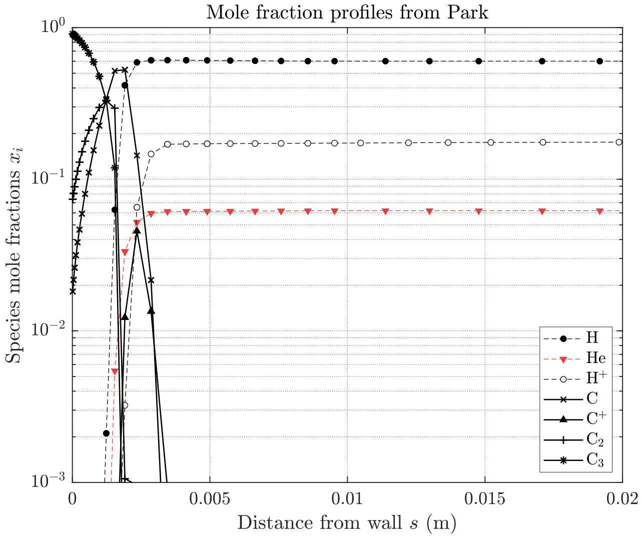

FIG. 24. Mole fractions from Park.[23]

To account for the presence of carbonaceous species in the ablation layer in the absence of a material-response code, the mole fractions obtained by Park were used, and are presented in Fig. 24. Hence, the analysis is limited to the species C, C^+, C_2, and C_3 since these are the only ones considered in the author's work. The stagnation line profile of species mole fractions obtained with SPARK was kept for $s > 0.3$ cm, where s is the distance to the wall, and the same gluing function used for the correction to the precursor heating mass fractions was applied between $0.2 < s < 0.3$ cm to continuously join the two solutions. Again, care was taken to ensure $\sum x_i = 1$ throughout the stagnation line. The resulting mole fraction profiles are shown in Fig. 25.

One important shortcoming of this approximation concerns the treatment of the ablation layer temperature. The injection of ablation species in the flowfield will reduce its temperature near the wall, and Park does not provide a temperature profile which could be employed as a correction. Hence, two possible limiting cases were analyzed. One of them considers the injection has no effect on the flowfield temperatures, and thus the temperature profile obtained with SPARK is kept unchanged. Otherwise, one may assume that the ablation products are injected at the wall temperature (3000 K), and the flowfield does not affect their temperature. Since the high pressure in the boundary layer promotes thermal equilibrium conditions, the flowfield temperatures were lowered to 3000 K for $s <$ 0.3 cm in this case.

Both conditions are compared to the original tangent-slab solution using the Gupta/Yos 2T case in Figs. 26(a) and 26(b). In the lower temperature scenario [Fig. 26(c)], the carbonaceous species at 3000 K near the wall absorb 42.1% of the original radiation impacting the stagnation point, reducing the radiative heating to 69.6 MW m^{-2}. This significant decline is essentially a result of continuum absorption due to C_2 and C_3 photoionization, along with the C_3 VUV band, all acting in the VUV region of the spectrum, which coincides with the domain of strongest emission due to atomic H lines and the H_2 band systems. Other C_2 band systems are

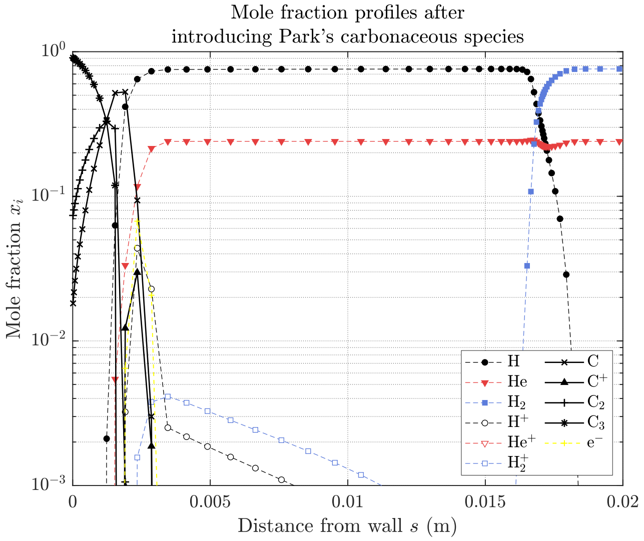

FIG. 25. Mole fractions used in the present work after Park's correction near the wall.

important in the visible range, adding a layer of absorption but also providing millions of spectral de-excitation jumps that contribute to line emission, albeit with a negligible influence on the total heat flux at this temperature.

As previously discussed, Park neglected several known radiative band systems. If only the systems used by the author are considered in the present case, the radiative heating is 69.1 MW m^{-2}, close to the value predicted when all systems are accounted for, indicating a negligible effect for the remaining systems at 3000 K.

A very different picture is obtained for the other limiting case. If the ablation products had a negligible impact on the boundary layer temperature, then the carbonaceous species' temperatures would rapidly increase to 20 000 K at its boundary, and emission from these radiative systems would instead increase the radiative heating (note that spallation, which would result in an additional radiation blockage process, is not taken into account in the present work). Figure 26(b) shows that the previously absorbing systems due to C_2 and C_3 transitions now significantly increase the radiative heating over that predicted originally. The heat fluxes obtained under these conditions are 890.7 MW m^{-2}, a 641% increase over the case without ablation products injection. Furthermore, the previously unimportant band systems in the visible range now comprise about a quarter of this increase.

Again, if only Park's systems are considered under these conditions, the radiative heat fluxes decrease to 851.9 MW m^{-2}, indicating the systems neglected by the author may have an important contribution at higher temperatures. However, this scenario is effectively unrealistic, since ablation layer temperatures are much closer to the 3000 K of the wall. In addition, even if the 20 000 K temperature was reached, dissociation of C_2 and C_3 would take place long before, decreasing their contributions substantially.

An additional comparison was performed taking into account the effects of ablation products injection together with precursor heating. The optimistic case was assumed (ablation layer at 3000 K), and the results are compared in Fig. 26(c) to the original precursor heating correction spectrum shown in Fig. 23. Not surprisingly, H_2 VUV radiation is now severely hindered due to C_2 and C_3 photoionization and C_3 VUV. In the visible range, several band systems contribute to line emission, although with a negligible impact on the overall radiative heating. The presence of these systems in the background of the strong atomic H lines observed in red also substantially reduces their contribution, and the total radiative heating is reduced to 154.1 MW m^{-2}, a 56.7% decrease when compared to the case with no ablation products.

Given the raise in emission observed in the nonconservative scenario, the possibility that the presence of carbonaceous species may help explain the intense heating observed at the shoulder was explored. In particular, the abundant C_3 molecule present in the high-temperature ablation layer at the stagnation region may absorb radiation here, then flow downstream toward the shoulder and release this stored energy at this location instead through radiative emission, increasing the radiative heat fluxes. A quick calculation places the flow residency time from the stagnation point to the shoulder at 7–14 μs along the boundary layer. Compared to estimated radiative de-excitation times of the C_3 VUV and C_3 Swings radiative systems, which are around 0.2 μs and 0.07 μs, respectively, the residency flow times are two orders of magnitude higher. Thus, any radiative energy absorbed at the stagnation region is rapidly emitted back to the flowfield, in a strongly coupled radiative flowfield.

6. Empirical correction for flowfield-radiation coupling

The so-called radiative cooling effect is captured by coupling the flow and radiation fields, including the radiative heat flux divergence term in the energy equation. Radiative energy is "lost" to the free-stream flow, and the shock-layer temperatures (in this, now, nonadiabatic flow) decrease as a result, leading to a cooling of the flow. The most widely used correlation for estimating the impact of radiative cooling on the radiative heating was developed by Tauber and Wakefield during preflight studies for the Galileo entry in Jupiter,[8] as the severe radiative heating expected during flight was anticipated to be extremely sensitive to this coupling effect. The radiative heat fluxes are corrected according to

$$q_{\mathrm{rad}}^{\mathrm{TW}} = \frac{q_{\mathrm{rad},\,0}}{1 + a\Gamma^{0.7}}, \tag{20}$$

where $q_{\mathrm{rad},0}$ is the uncoupled radiative flux, a is a parameter depending on the atmosphere ($a = 3$ for Jupiter's case), and Γ depends on the free-stream density and velocity, according to

$$\Gamma = 4q_{\mathrm{rad},\,0}/\rho_\infty V_\infty^3. \tag{21}$$

Correlations such as the Tauber-Wakefield, which depend on the local radiative heat flux, are known to underestimate the radiative cooling effect at downstream regions, due to its nonlocal character. Radiatively cooled gas at the strongly radiating stagnation region flows downstream and reduces the temperature, an effect that the correlation is unable to capture. Thus, the decrease in radiative heating expected after the correction is greater at the stagnation region than at the shoulder.

This is indeed observed in Fig. 27. The decrease in radiative heating is significant all along the body, but more so in the stagnation

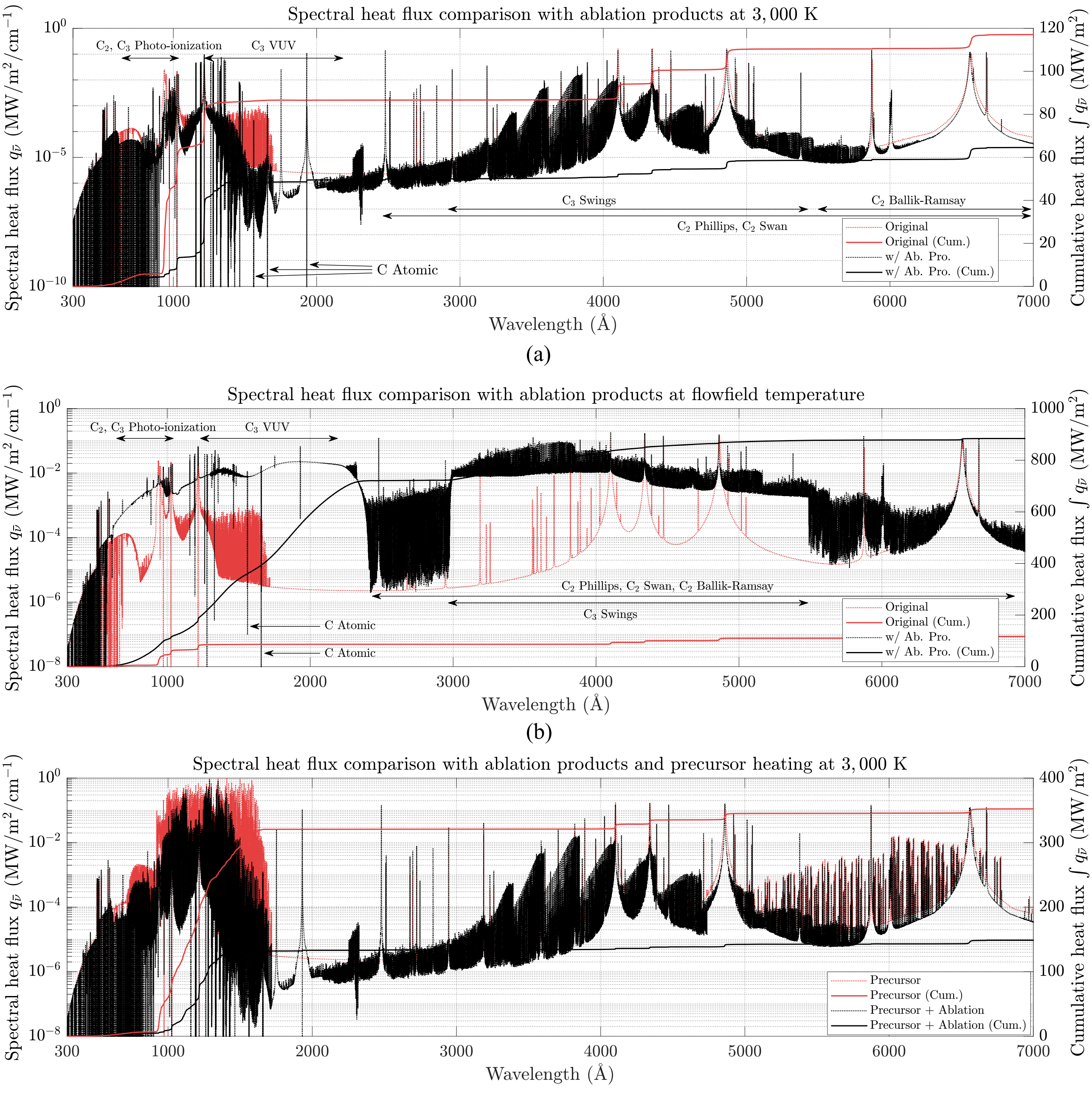

FIG. 26. Spectral heat flux comparisons when ablation products are added to the radiative analysis. (a) Limiting case 1: ablation products and flowfield at 3000 K for $s < 0.3$ cm. (b) Limiting case 2: flowfield temperatures kept unchanged from SPARK. (c) Precursor corrections with ablation products using limiting case 1 (3000 K for $s < 0.3$ cm).

region. Although the radiative heat fluxes predicted in the present work are, in general, higher than those predicted by previous authors, inclusion of radiative cooling effects, albeit in an approximate fashion, is shown to reduce these figures to values found in the literature. The results of Moss and Simmonds for the altitudes of 184.5 km (40 s) and 166.6 km (43 s) underpredict the heat fluxes at the spherical region of the probe, given that the trajectory point studied in the present work lies between the two. However, the opposite is true toward the shoulder. Several factors may have contributed to this disparity, the most important being the chemical

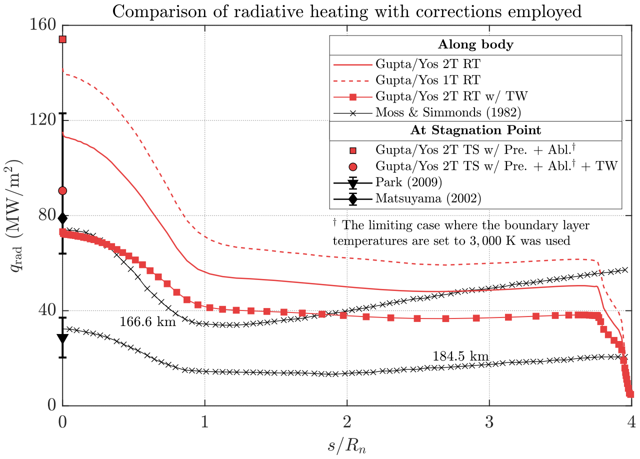

FIG. 27. Comparison of radiative heat flux results along body wall with literature.

equilibrium assumption employed and the Wilke transport model used. The stagnation point prediction is within the bounds reported by Matsuyama for the same altitudes, which were obtained using a coupled tangent-slab approach, but only considering H and H^+ radiation and thermochemical equilibrium. Park's prediction, which properly treats ablation products injection, is significantly lower, but again an equilibrium assumption was used. It is difficult to provide a meaningful comparison with previous studies on radiation since these rely on a thermochemical equilibrium flowfield, a simplification that significantly departs from the chemical nonequilibrium actually present during flight. Thermal nonequilibrium also plays an important role, especially at higher altitudes such as in the case studied in the present work, due to H_2 emission at the shock.

Two additional points were included at the stagnation point in Fig. 27. Both show how the combined effects of precursor heating and ablation products absorption tend to result in an increase in radiative heating due to precursor heating emission. When precursor heating and ablation injection are accounted for in the Gupta/Yos 2T case, the heat flux at the stagnation point rises to 154.1 MW m^{-2}, a 33.7% increase due to these corrections. Furthermore, when the Tauber-Wakefield correlation is applied, the heat fluxes increase from 73.2 MW m^{-2} to 90.4 MW m^{-2} after precursor heating and ablation injection effects are considered at the stagnation point, a 23.5% increase.

Finally, the results obtained in the present work are summarized in Table VII. The convective heating results only vary for the first four rows, and thus, these are the only ones presented. The radiative heating, on the other hand, was subject to extensive sensitivity studies, making up most of the table. The influence of precursor heating and ablation products was only possible to study at the stagnation point, due to the nature of the approximations employed.

V. CONCLUSIONS

Upon the implementation of a new transport property architecture within SPARK, which allows the Gupta/Yos model to be applied to any Solar System atmosphere, a comparison with the Wilke/Blottner/Eucken transport model revealed the shortcomings of the latter in the context of H_2–He mixtures. When applied to Galileo's entry, it overpredicts the maximum shock temperature and underestimates its thickness. No definitive conclusions could be drawn regarding its influence on the convective heating when compared to the Gupta/Yos model, due to a poor boundary layer resolution, even with the finest mesh studied. Nonetheless, the Gupta/Yos results predict convective heat fluxes exceeding 100 MW m^{-2} at the stagnation point and about 60% lower values over the conical frustum. Thermal equilibrium and nonequilibrium solutions were also found to match in terms of convective heating.

The same cannot be said regarding radiative heating, where H_2 was found to play a significant role, especially when precursor heating effects were accounted for. Using Tiwari *et al.*'s stagnation line solution as a guideline, a 208% increase in radiative heat flux was observed. Therefore, the influence of H_2 radiation in future missions to Jupiter must be accounted for. Results from other sensitivity studies performed on radiative heating also reveal the following:

- Good agreement between tangent-slab and ray-tracing models, with a maximum 10% difference at the stagnation point.
- The absorption effectiveness of ablation products in the VUV range may be impaired due to intense emission from C_2 and C_3 photorecombination, as well as the C_3 VUV system. Estimates based on different assumptions for the boundary layer temperatures lead to radiative heat fluxes that vary from −40% (decrease) to over 670% (increase) when compared to the baseline solution obtained with the most accurate model used. Without a flowfield coupled to a material response code, it is hard to predict the effect that ablation products have when present in the shock layer.
- An increase in radiative heating appears to result from the combined effect of precursor heating and ablation.

Finally, the improved directional discretization scheme implemented in SPARK LbL's ray-tracing algorithm was shown to provide reasonable accuracy (within 5%) with just 50 rays for the Galileo entry case. However, the good agreement obtained with the tangent-slab model still justifies its use for preliminary analysis due to the reduced computational cost.

ACKNOWLEDGMENTS

M. Lino da Silva's work has been funded by the Portuguese FCT–Fundação para a Ciência e Tecnologia through the Project No. UID/FIS/50010/2019. The authors would like to thank Markus Fertig for the thoughtful suggestions regarding the modeling of shoulder expansion and Domenico Bruno for general comments about this work, provided during the European Space Agency-sponsored 8th International Workshop on Radiation of High Temperature Gases.

REFERENCES

[1] P. Reynier, G. D'Ammando, and D. Bruno, "Modelling chemical kinetics and convective heating in giant planet entries," Prog. Aerosp. Sci. **96**, 1–22 (2018).
[2] F. S. Milos, Y.-K. Chen, T. Squire, and R. Brewer, "Analysis of Galileo probe heatshield ablation and temperature data," J. Spacecr. Rockets **36**, 298–306 (1999).

[3] J. O. Arnold, "Planetary entry probes 1953–2036: A technologist's perspective," in 10th International Planetary Probe Workshop, 2013.

[4] B. Lopez and M. Lino Da Silva, "SPARK: A software package for aerodynamics, radiation and kinetics," in *46th AIAA Thermophysics Conference* (AIAA, 2016), p. 4025.

[5] M. Lino da Silva, B. Lopez, and S. Espinho, SPARTAN 2.6 User's Manual, 2016.

[6] M. Lino da Silva, "An adaptive line-by-line—Statistical model for fast and accurate spectral simulations in low-pressure plasmas," J. Quant. Spectrosc. Radiat. Transfer **108**, 106–125 (2007).

[7] M. Lino da Silva, "The line-by-line radiative code spartan" (2016), http://esther.ist.utl.pt/spartan/; accessed 24 May 2019.

[8] M. E. Tauber and R. M. Wakefield, "Heating environment and protection during Jupiter entry," J. Spacecr. Rockets **8**, 630–636 (1971).

[9] M. Perrin, G. Colonna, G. D'Ammando, L. Pietanza, P. Riviere, A. Soufani, and S. Surzhikov, "Radiation models and radiation transfer in hypersonics," Open Plasma Phys. J. **7**, 114–126 (2014).

[10] L. P. Leibowitz, "Measurements of the structure of an ionizing shock wave in a hydrogen-helium mixture," Phys. Fluids **16**, 59–68 (1973).

[11] F. R. Livingston and P. Y. Poon, "Relaxation distance and equilibrium electron density measurements in hydrogen-helium plasmas," AIAA J. **14**, 1335–1337 (1976).

[12] L. P. Leibowitz and T.-J. Kuo, "Ionizational nonequilibrium heating during outer planetary entries," AIAA J. **14**, 1324–1329 (1976).

[13] J. N. Moss, "A study of the aerothermal entry environment for the Galileo probe," in *Entry Heating and Thermal Protection* (AIAA, 1980), pp. 3–25.

[14] J. N. Moss, J. J. Jones, and A. L. Simmonds, "Radiative flux penetration through a blown shock layer for Jupiter entry conditions," in *Outer Planet Entry Heating and Thermal Protection* (AIAA, 1978), pp. 22–41.

[15] J. N. Moss, A. L. Simmonds, and E. C. Anderson, "Turbulent radiating shock layers with coupled ablation injection," J. Spacecr. Rockets **17**, 177–183 (1980).

[16] J. Moss and A. Simmonds, "Galileo probe forebody flowfield predictions during Jupiter entry," in *3rd Joint Thermophysics, Fluids, Plasma and Heat Transfer Conference* (AIAA, 1982), p. 874.

[17] S. N. Tiwari and K. Y. Szema, "Effects of precursor heating on chemical and radiative nonequilibrium viscous flow around a Jovian entry body," in *2nd Thermophysics and Heat Transfer Conference* (AIAA, 1978), Vol. 64.

[18] S. Matsuyama, N. Ohnishi, A. Sasoh, and K. Sawada, "Numerical simulation of Galileo probe entry flowfield with radiation and ablation," J. Thermophys. Heat Transfer **19**, 28–35 (2005).

[19] S. Matsuyama, Y. Shimogonya, N. Ohnishi, K. Sawada, and A. Sasoh, "Numerical simulation of Galileo probe entry flowfield with radiation," in *8th AIAA/ASME Joint Thermophysics and Heat Transfer Conference* (AIAA, 2002).

[20] C. Park, "Injection-induced turbulence in stagnation-point boundary layers," AIAA J. **22**, 219–225 (1984).

[21] M. Furudate, I.-S. Jeung, and S. Matsuyama, "Nonequilibrium calculation of flowfield over Galileo probe," in *44th AIAA Aerospace Sciences Meeting and Exhibit* (AIAA, 2006), Vol. 7.

[22] C. Park, "Effect of Lymann radiation on nonequilibrium ionization of atomic hydrogen," in *37th AIAA Thermophysics Conference* (AIAA, 2004), Chap. 2277.

[23] C. Park, "Stagnation-region heating environment of the Galileo probe," J. Thermophys. Heat Transfer **23**, 417–424 (2009).

[24] P. Reynier, "Numerical reconstruction of Galileo entry," in 5th International Workshop on Radiation and High Temperature Gases in Atmospheric Entry, 2012.

[25] G. D'Ammando, M. Capitelli, F. Esposito, A. Laricchiuta, L. D. Pietanza, and G. Colonna, "The role of radiative reabsorption on the electron energy distribution functions in H_2/He plasma expansion through a tapered nozzle," Phys. Plasmas **21**, 093508 (2014).

[26] G. Colonna, G. D'Ammando, L. Pietanza, and M. Capitelli, "Excited-state kinetics and radiation transport in low-temperature plasmas," Plasma Phys. Controlled Fusion **57**, 014009 (2015).

[27] H. Yee, R. Warming, and A. Harten, "Implicit total variation diminishing (TVD) schemes for steady-state calculations," J. Comput. Phys. **57**, 327–360 (1985).

[28] H. Yee, "Upwind and symmetric shock-capturing schemes," Technical Report NASA-TM-89464, NASA, 1987.

[29] M. Furudate, "Nonequilibrium calculation of high-temperature radiating H_2-He flowfield," J. Thermophys. Heat Transfer **23**, 651–659 (2009).

[30] J. D. Anderson, *Hypersonic and High-Temperature Gas Dynamics*, 2nd ed. (AIAA Education, AIAA, 2006).

[31] W. G. Vincenti and C. H. Kruger, *Introduction to Physical Gas Dynamics*, 1st ed. (John Wiley and Sons, 1965).

[32] U. Fantz and D. Wünderlich, "Franck–Condon factors, transition probabilities and radiative lifetimes for hydrogen molecules and their isotopomeres," Technical Report INDC(NDS)-457, IAEA, 2004.

[33] K.-P. Huber and G. Herzberg, *Constants of Diatomic Molecules* (Van Nostrand Reinhold, New York, 1979).

[34] A. Kramida, Y. Ralchenko, J. Reader, and N. A. Team, "NIST atomic spectra database (version 5.5.6)" (2018), https://physics.nist.gov/asd; accessed: 10 May 2018.

[35] G. Palmer, D. Prabhu, and B. A. Cruden, "Aeroheating uncertainties in Uranus and Saturn entries by the Monte Carlo method," J. Spacecr. Rockets **51**, 801–814 (2014).

[36] F. Thivet, M. Perrin, and S. Candel, "A unified nonequilibrium model for hypersonic flows," Phys. Fluids A **3**, 2799–2812 (1991).

[37] J. E. Dove and H. Teitelbaum, "The vibrational relaxation of H_2. I. Experimental measurements of the rate of relaxation by H_2, He, Ne, Ar, and Kr," Chem. Phys. **6**, 431–444 (1974).

[38] J. G. Kim, O. J. Kwon, and C. Park, "Master equation study and nonequilibrium chemical reactions for H + H_2 and He + H_2," J. Thermophys. Heat Transfer **23**, 443–453 (2009).

[39] J. Kim, O. Kwon, and C. Park, "State-to-state rate coefficients and master equation study for H_2 + H_2," in *47th AIAA Aerospace Sciences Meeting including The New Horizons Forum and Aerospace Exposition* (AIAA, 2009), p. 1023.

[40] D. Bruno, C. Catalfamo, M. Capitelli, G. Colonna, O. De Pascale, P. Diomede, C. Gorse, A. Laricchiuta, S. Longo, D. Giordano *et al.*, "Transport properties of high-temperature Jupiter atmosphere components," Phys. Plasmas **17**, 112315 (2010).

[41] D. Bruno, M. Capitelli, C. Catalfamo, R. Celiberto, G. Colonna, P. Diomede, D. Giordano, C. Gorse, A. Laricchiuta, S. Longo, D. Pagano, and F. Pirani, "Transport properties of high-temperature Mars-atmosphere components," Technical Report STR-256, European Space Agency, 2008.

[42] G. E. Palmer and M. J. Wright, "Comparison of methods to compute high-temperature gas viscosity," J. Thermophys. Heat Transfer **17**, 232–239 (2003).

[43] G. Palmer and M. Wright, "A comparison of methods to compute high-temperature gas thermal conductivity," in *36th AIAA Thermophysics Conference* (AIAA, 2003), p. 3913.

[44] C. Wilke, "A viscosity equation for gas mixtures," J. Chem. Phys. **18**, 517–519 (1950).

[45] F. G. Blottner, M. Johnson, and M. Ellis, "Chemically reacting viscous flow program for multi-component gas mixtures," Technical Report SC-RR-70-754, Sandia Labs., Albuquerque, New Mexico, 1971.

[46] R. N. Gupta, J. M. Yos, R. A. Thompson, and K.-P. Lee, "A review of reaction rates and thermodynamic and transport properties for an 11-species air model for chemical and thermal nonequilibrium calculations to 30000 K," Technical Report NASA-RP-1232, NASA, 1990.

[47] J. M. Yos, "Approximate equations for the viscosity and translational thermal conductivity of gas mixtures," Technical Report AVSSD-0112-67-RM, AVCO Corporation, Wilmington, Massachusetts, 1967.

[48] I. A. Sokolova, "Collision integrals for components of high-temperature hydrogen-helium mixture," Teplofiz. Vys. Temp. **15**, 734–743 (1977), original document in Russian.

[49] L. Biolsi, Jr., "Transport properties in the atmosphere of Jupiter," Technical Report NASA-CR-158094, NASA, 1978.

[50] D. Bruno, C. Catalfamo, M. Capitelli, G. Colonna, P. Diomede, C. Gorse, A. Laricchiuta, S. Longo, F. Pirani *et al.*, "Transport properties of high-temperature Jupiter-atmosphere components," Technical Report STR-256, European Space Agency, 2008.

[51] M. Capitelli, D. Cappelletti, G. Colonna, C. Gorse, A. Laricchiuta, G. Liuti, S. Longo, and F. Pirani, Chem. Phys. **338**(1), 62–68 (2007).

[52] M. J. Wright, D. Bose, G. E. Palmer, and E. Levin, "Recommended collision integrals for transport property computations. Part 1: Air species," AIAA J. **43**, 2558–2564 (2005).

[53] L. Biolsi, "Transport properties in the Jovian atmosphere," J. Geophys. Res.: Space Phys. **83**, 1125–1131, https://doi.org/10.1029/ja083ia03p01125 (1978).

[54] B. McBride and S. Gordon, "Computer program for calculation of complex chemical equilibrium compositions and applications II. Users manual and program description," Technical Report NASA-RP-1311, NASA, 1996.

[55] C. O. Johnston, "Nonequilibrium shock-layer radiative heating for Earth and Titan entry," Ph.D. thesis, Virginia Tech, 2006.

[56] H. Griem, *Spectral Line Broadening by Plasmas*, 1st ed. (Elsevier, 2012).

[57] A. Döhrn, P. Nowack, A. Könies, S. Günter, and V. Helbig, "Stark broadening and shift of the first two Paschen lines of hydrogen," Phys. Rev. E **53**, 6389 (1996).

[58] T. Wujec, A. Jazgara, J. Halenka, and J. Musielok, "Stark broadening of the hydrogen Paschen γ transition at electron densities of the order of cm," Eur. Phys. J. D **23**, 405–408 (2003).

[59] C. Stehlé and S. Fouquet, "Hydrogen Stark broadened Brackett lines," Int. J. Spectrosc. **2010**, 1.

[60] K. Pachucki and J. Komasa, "Nonadiabatic corrections to rovibrational levels of H_2," J. Chem. Phys. **130**, 164113 (2009).

[61] H. Abgrall, E. Roueff, F. Launay, J.-Y. Roncin, and J.-L. Subtil, "The Lyman and Werner band systems of molecular hydrogen," J. Mol. Spectrosc. **157**, 512–523 (1993).

[62] H. M. Crosswhite, *The Hydrogen Molecule Wavelength Tables of Gerhard Heinrich Dieke* (Wiley-Interscience, 1972).

[63] D. Bailly, E. Salumbides, M. Vervloet, and W. Ubachs, "Accurate level energies in the $EF^1\Sigma_g^+$, $GK^1\Sigma_g^+$, $H^1\Sigma_g^+$, $B^1\Sigma_u^+$, $C^1\Pi_u$, $B'^1\Sigma_u^+$, $D^1\Pi_u$, $I^1\Pi_g$, $J^1\Delta_g$ states of H_2," Mol. Phys. **108**, 827–846 (2010).

[64] TOPBase: Online Atomic Database (2019) http://cdsweb.u-strasbg.fr/topbase/topbase.html; accessed 10 March 2019.

[65] T. Ohmura and H. Ohmura, "Electron-hydrogen scattering at low energies," Phys. Rev. **118**, 154–157 (1960).

[66] A. M. Frolov, "On the absorption of radiation by the negatively charged hydrogen ion. I. General theory and construction of the wave functions," preprint arXiv:1110.3432 (2011).

[67] C. Ramsbottom and K. Bell, "Photodetachment cross sections for the 1s2s2p metastable state of the negative helium ion," J. Phys. B: At., Mol. Opt. Phys. **32**, 1315–1333 (1999).

[68] J. A. R. Samson and G. N. Haddad, "Total photoabsorption cross sections of H_2 from 18 to 113 eV," J. Opt. Soc. Am. B **11**, 277–279 (1994).

[69] M. Yan, H. Sadeghpour, and A. Dalgarno, "Photoionization cross sections of He and H_2," Astrophys. J. **496**, 1044–1050 (1998).

[70] M. Yan, H. Sadeghpour, and A. Dalgarno, "Erratum: Photoionization cross sections of He and H_2," Astrophys. J. **559**, 1194 (2001).

[71] W. F. Huebner and W. D. Barfield, *Opacity, Astrophysics and Space Science Library* (Springer, 2014).

[72] A. Heays, A. Bosman, and E. van Dishoeck, "Photodissociation and photoionisation of atoms and molecules of astrophysical interest," Astron. Astrophys. **602**, A105 (2017).

[73] H. Abgrall, E. Roueff, and I. Drira, "Total transition probability and spontaneous radiative dissociation of B, C, B′ and D states of molecular hydrogen," Astron. Astrophys., Suppl. Ser. **141**, 297–300 (2000).

[74] S. Geltman, "Free-free radiation in electron-neutral atom collisions," J. Quant. Spectrosc. Radiat. Transfer **13**, 601–613 (1973).

[75] S. Chauveau, "Constitution de bases de données spectroscopiques relatives à un plasma d'air: Application au calcul de transferts radiatifs," Ph.D. thesis, Châtenay-Malabry, Ecole centrale de Paris, 2001.

[76] T. John, "Neutral bremsstrahlung from molecular hydrogen and nitrogen," Astron. Astrophys. **67**, 395–398 (1978).

[77] A. M. Brandis, B. A. Cruden, T. R. White, D. A. Saunders, and C. O. Johnston, "Radiative heating on the after-body of Martian entry vehicles," in *45th AIAA Thermophysics Conference* (AIAA, 2015), p. 3111.

[78] C. O. Johnston and A. M. Brandis, "Features of afterbody radiative heating for Earth entry," in *11th AIAA/ASME Joint Thermophysics and Heat Transfer Conference* (AIAA, 2014), p. 2675.

[79] C. O. Johnston, "Influence of radiative absorption on non-Boltzmann modeling for Mars entry," J. Thermophys. Heat Transfer **28**, 795–799 (2014).

[80] C. O. Johnston and A. Mazaheri, "Impact of non-tangent-slab radiative transport on flowfield-radiation coupling," J. Spacecr. Rockets **55**, 899–913 (2018).

[81] Á. González, "Measurement of areas on a sphere using Fibonacci and latitude–longitude lattices," Math. Geosci. **42**, 49 (2010).

[82] G. J. Elbert and P. Cinnella, "Truly two-dimensional algorithms for radiative heat transfer calculations in reactive flows," Comput. Fluids **24**, 523–552 (1995).

[83] M. Lino Da Silva and J. Beck, "Contribution of CO_2 IR radiation to Martian entries radiative wall fluxes," in *49th AIAA Aerospace Sciences Meeting Including the New Horizons Forum and Aerospace Exposition* (AIAA, 2011), p. 135.

[84] J. Beck, P. Omaly, M. Lino da Silva, and S. Surzhikov, "Radiative heating of the exomars entry demonstrator module," in 7th European Symposium on Aerothermodynamics, 2011.

[85] C. O. Johnston, P. A. Gnoffo, and A. Mazaheri, "Influence of coupled radiation and ablation on the aerothermodynamic environment of planetary entry vehicles," in *Radiation and Gas-Surface Interaction Phenomena in High Speed Re-entry* (2013); available at https://www.vki.ac.be/index.php/component/jevents/eventdetail/312/-/sto-avt-218-radiation-and-gas-surface-interaction-phenomena-in-high-speed-re-entry?Itemid=816.

[86] M. Lino da Silva, "Simulation des propriétés radiatives du plasma entourant un véhicule traversant une atmosphère planétaire à vitesse hypersonique—Application à la planète Mars," Ph.D. thesis, Université d'Orléans, 2004.

[87] M. Lino da Silva, "Arrays of radiative transition probabilities for CO_2–N_2 plasmas," J. Quant. Spectrosc. Radiat. Transfer **102**, 348–386 (2006).

[88] T. Furtenbacher, I. Szabó, A. G. Császár, P. F. Bernath, S. N. Yurchenko, and J. Tennyson, "Experimental energy levels and partition function of the $^{12}C_2$ molecule," Astrophys. J., Suppl. Ser. **224**, 44 (2016).

[89] P. J. Bruna and F. Grein, "Spectroscopy of the C_2 molecule: Valence and Rydberg states in the 7-10 eV region. An *ab initio* study," Can. J. Phys. **79**, 653–671 (2001).